Geochronology, pyrite trace elements, and in-situ S isotopes of the giant Nagengkangqie'er silver deposit in the Eastern Kunlun Orogenic Belt, Northern Tibetan Plateau

Xin-Ming Zhang [a,b], Yan-Jun Li [a,*], Sheng-Tao Zhang [a], Wei-Wei Li [a], Chong-Wen Xu [a], Andreas Kamradt [b], Gregor Borg [b], Jun-Hao Wei [a,*]

[a] School of Earth Resource, China University of Geoscience, Wuhan 430074, China
[b] Institute of Geosciences and Geography, Martin Luther University Halle-Wittenberg, Halle (Saale) 06120, Germany

ARTICLE INFO

ABSTRACT

The Nagengkangqie'er (Nageng) silver deposit, situated in the Eastern Kunlun Orogenic Belt (EKOB), Northwestern China. It contains 5,070 tons of contained silver at a silver grade of 325 g/t. Nonetheless, the genesis of the Nageng silver deposit is still under debate, due to the absence of definitive constraints the mineralization age and the metal sources. The U-Pb data analysis of a post-ore calcite vein established the minimum age of the mineralization at 207 ± 3 Ma, whereas the maximum age of 217 ± 4 Ma was determined from zircon U-Pb data obtained from the altered and mineralized rhyolitic porphyry host-rock. These temporal limitations suggest that the mineralization formed at ca. 217–207 Ma, and it is associated with the post-collisional setting of the Paleo-Tethys evolution in the EKOB. The distinct textural patterns, as revealed by petrographic observations, suggest three types of pyrites: py1 is composed of euhedral pyrite in the early barren quartz vein at stage 1, py2 is represented by subhedral-anhedral grains in massive ore veins at stage 2, and py3 forms euhedral crystals of varying sizes, which are interspersed with early-formed marcasite in the quartz + calcite + silver-bearing sulfosalt-dominated veins at stage 3. In-situ $\delta^{34}S$ values of pyrites range between −2.33 ‰ and −0.37 ‰, indicating a dominantly magmatic origin. EPMA studies have revealed that silver in the Nageng deposit predominantly occurs as silver-bearing galena at stage 2, whereas silver is enriched in sulfosalts of stage 3. From py1 to py3, a decrease in the Co-content indicates a decrease in the ore-forming fluid temperatures. The presence of stage 3 sulfide, sliver-bearing sulfosalt, and calcite-quartz in a fracture-filled vein indicates low-pressure conditions during its formation, compared to stages 1 and 2. In summary, the Nageng deposit is a typical magmatic-hydrothermal vein-type Ag-Pb-Zn deposit. Fluid cooling and decrease in pressure, coupled with decreases in fO_2 and fS_2, are the parameters inferred to have led to a decrease of silver solubility in the hydrothermal fluids and, successively, promoted extensive Ag deposition.

1. Introduction

Hydrothermal vein-type Ag-Pb-Zn deposits are highly valued for their economic significance due to their high-grade silver content, which occurs as silver-bearing sulfosalts, in association with base metals such as lead and zinc (Simmons et al., 2005; Borojević Šoštarić et al., 2011, Borojević Šoštarić et al., 2013; Li et al., 2019; Li et al., 2020a). Furthermore, these deposits have the potential to serve as substantial reservoirs of these metals (Baumgartner et al., 2008; Mango et al., 2014; Zhai et al., 2019; Zhai et al., 2020). This type of deposits is commonly associated with magmatic-hydrothermal systems and are generally found in continental rifts, volcanic arcs, and collisional orogens (Haynes, 1993; Jean-Philippe et al., 2012; Mao et al., 2013a; Jiang et al., 2015; Jansson et al., 2017). Accurately determining mineralization ages is of paramount importance in unraveling the intricate relationship between ore genesis and geotectonic events (Fan et al., 2014; Mederer et al., 2014; Yan et al., 2021; Kouhestani et al., 2022). Nonetheless, dating vein-type Ag-Pb-Zn deposits has posed a formidable challenge

due to the absence of minerals that unequivocally associate with silver deposition and are suitable for radiogenic isotope techniques (Zhai et al., 2017; Benites et al., 2022; Li et al., 2022). Furthermore, subsequent hydrothermal activities subsequent to ore formation could potentially disturb the isotopic systematics of minerals, thereby introducing additional complexity into the chronological assessment (Corral, 2020; Jin et al., 2021).

Calcite is a prevalent gangue mineral in various types of hydrothermal deposits (Grandia et al., 2000; Zhang et al., 2020; Jin et al., 2021). In recent years, in situ U-Pb isotopic analyses have been conducted using laser ablation inductively coupled plasma mass spectrometry (LA-ICP-MS) with ion counters, offering the potential to date these carbonates (e.g., Kurumada et al., 2020; Su et al., 2021; Pavlovskaia et al., 2022). This technique has proven successful in dating numerous ore deposits, such as antimony mineralization in South China (Sheng et al., 2022; Xu et al., 2022), five-element vein deposits in central Germany (Kreissl et al., 2018), and Carlin-type gold deposits in central Yukon, Canada (Pinet et al., 2022). Additionally, pyrite, which is the dominant auriferous sulfide in the vein type Ag-Pb-Zn deposit (Paiement et al., 2012; Mao et al., 2013b; Stouraiti et al., 2019; Ishida et al., 2022), is observed throughout the mineralization process. The association and distribution of trace elements in pyrite have been confirmed to provide

crucial insights into the source of metals and the physicochemical conditions of the ore-forming fluids (Vaughan, 2006; Börner et al., 2021; Li et al., 2023b).

The Eastern Kunlun orogenic belt (EKOB) in NW China is a well-known mineralized belt with a significant exploration and mining history (Zhao et al., 2021a; Deng et al., 2022). The recent discovery of the Nagengkangqie'er (Nageng) Ag deposit, the first giant silver deposit found in the EKOB, has garnered considerable attention from researchers and explorers. The deposit geology (Chen et al., 2021; Li et al., 2017; Xu et al., 2014), geochronology of magmatism (Chen et al., 2021, 2022a; Guo et al., 2019), geochemistry (Xu et al., 2020; Chen et al., 2022b), and fluid inclusions (FIs) (Li and Li, 2017; Chen et al., 2019) have been extensively investigated in the past decade. However, several crucial issues still require additional investigation. One of these crucial critical issues is the timing of the Ag mineralization, making it difficult to establish a temporal link between ore formation and evolution of the EKOB. Additionally, ongoing debates persist regarding the metal sources and the mechanism of metal precipitation.

In this investigation, we identified and dated post-ore calcite, using LA-ICP-MS in combination with the U-Pb age of wall rock zircon to establish a reliable timeframe for the silver mineralization in Nageng. Additionally, in order to further characterize the hydrothermal fluid
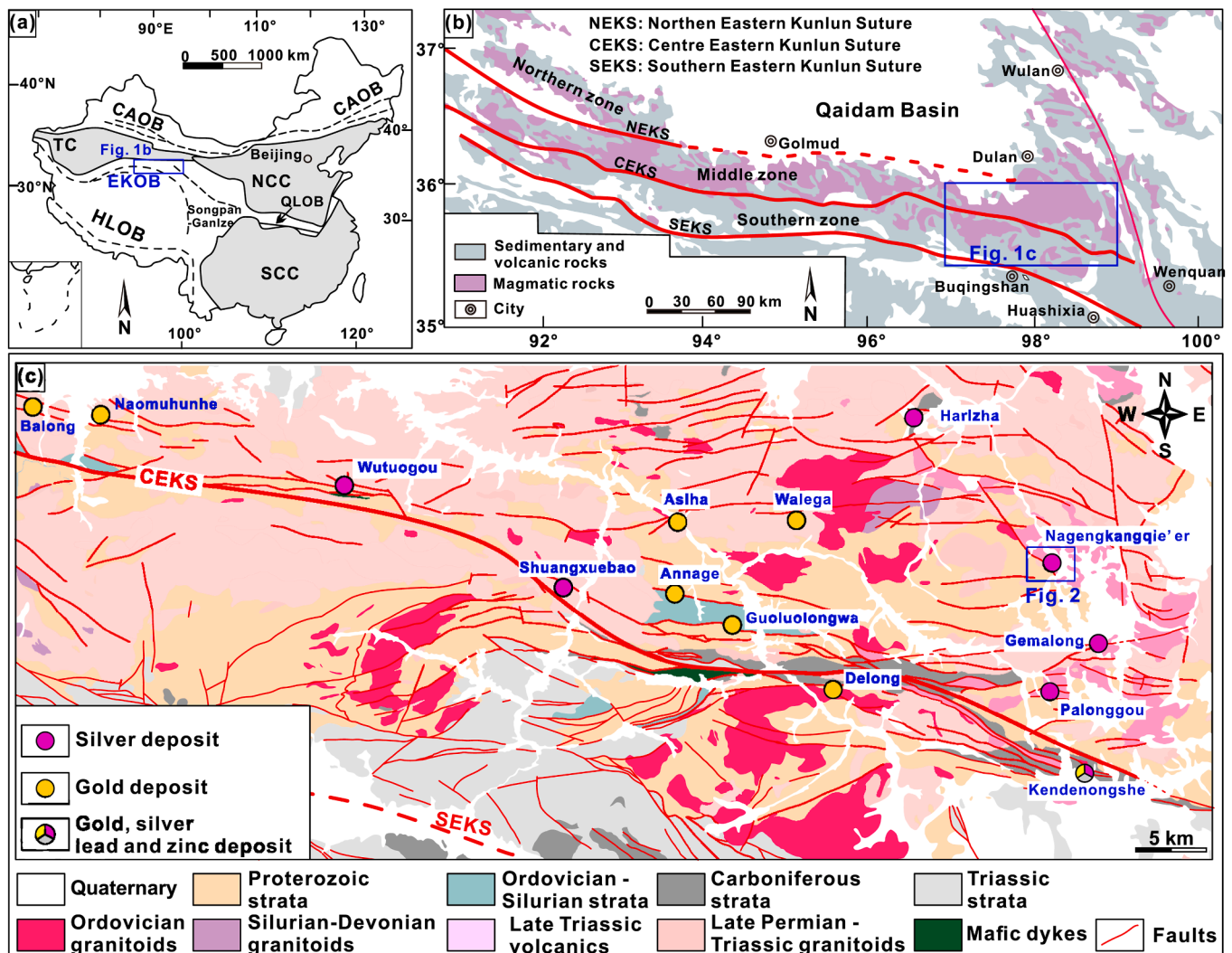

Fig. 1. (a) Tectonic map of China showing the location of the EKOB (modified after Li et al., 2020c). (b) The tectonic map showing the dominated terranes of the EKOB and the location of Gouli ore field (modified after Pan et al., 2012; Chen et al., 2017). (c) Geological map of the Gouli ore field showing the distribution of the main silver and gold deposits (modified after Chen et al., 2020; Zhao et al., 2021b). (CAOB = Central Asia Orogenic Belt; TC = Tarim Craton, EKOB = Eastern Kunlun Orogenic Belt, NCC = North China Craton, SCC = South China Craton, QLOB = Qinling Orogenic Belt, HLOB = Himalayan Orogenic Belt).

sources and metal formation conditions, we conducted in-situ pyrite chemical, S isotopic, and electron probe microscopy (EPM) analyses on sulfides and silver minerals. Our overarching objective was to provide a more comprehensive understanding of the Nageng Ag deposit in the EKOB. Furthermore, we aimed to contribute to the ongoing efforts in resolving the age of silver mineralization by employing calcite dating techniques.

2. Regional Geological setting

The EKOB is situated on the northern margin of the Tibetan Plateau, representing the western portion of the Central China Orogen (Fig. 1a; Pan et al., 2012; Dong et al., 2022). The EKOB consists of three distinct tectonic divisions known as the Northern, Middle, and Southern Kunlun terranes. These divisions are delineated by the Central and Southern Eastern Kunlun Sutures (Fig. 1b; Chen et al., 2012; Li et al., 2020b). The EKOB has undergone multiple orogenic events associated with the evolution of the Neoproterozoic to Early Paleozoic Proto-Tethys Ocean and the Late Paleozoic to Mesozoic Paleo-Tethys Ocean (Dai et al., 2013; Zhong et al., 2017; Li et al., 2021a). It is noteworthy that a significant proportion of deposits within the EKOB can be traced back to the development of the Paleo-Tethys Ocean (Zhao et al., 2021b; Zhang et al., 2023). Therefore, the tectonic evolution of the Paleo-Tethys Ocean in the EKOB since the Paleozoic can be summarized as follows: 1) Subduction of the Paleo-Tethys Ocean began in the Early Permian, with subsequent episodes of back-arc extension during the Late Permian to Early Triassic (Chen et al., 2017; Zhao et al., 2019; Wang et al., 2020; Li et al., 2020b). 2) Continental collision ensued during the Middle Triassic (Chen et al., 2021; Kamaunji et al., 2020; Li et al., 2021a). Following the Late Triassic period, the EKOB entered an extensional regime attributed to lithospheric delamination (Hu et al., 2016; Zhou et al., 2020; Huang et al., 2021; Yu et al., 2020).

The Gouli orefield is located on the eastern segment of the EKOB (Fig. 1b) and is crossed by the Central East Kunlun Suture Zone (CEKS). This area exclusively encompasses the Paleoproterozoic Jinshuikou Group (composed of gneiss, amphibolite, and marble). Overlying the Jinshuikou Group are the Naij Tai Group (composed of *meta*-volcanic and *meta*-sedimentary rocks), as well as Carboniferous-Triassic sedimentary and volcanic rocks (Fig. 1c). These rocks have been intruded by Ordovician-Silurian granitoids, Permian-Triassic arc granitoids, and Middle to Late Triassic syn-collision and post-collision granitic rocks, along with locally occurring mafic rocks (Fig. 1c; Dong et al., 2018; Huang, 2021). The Gouli orefield hosts more than ten gold and silver deposits, including the Guoluolongwa (>40 t Au), Walega (>16 t Au), Annage (>8 t Au), Asiha (>6 t Au), Kendenongshe (>40 t Au and > 600 t Ag), and Nageng (>5000 t Ag), indicating a significant potential for exploration of Au and Ag in the EKOB (Chen et al., 2020; Li et al., 2021b; Zhao et al., 2021b).

3. Ore deposit geology, mineralization and alteration

3.1. Deposit geology

The Nageng silver deposit, which is located in the Eastern segment of the Gouli orefield (Fig. 1c), has a total reserve of 5,070 metric tons (t) of contained silver with an average grade of 325 g/t (Guo, 2020; Chen et al., 2022b). Ore bodies are hosted by a sequence of metamorphic and volcanic rocks, covered by Quaternary sediments (Fig. 2a). The metamorphic rocks belong to the Proterozoic Jinshuikou Group and comprise biotite-amphibole-plagioclase gneisses and hornblende schists. Volcanic rocks comprise the Middle Triassic Naocangjiangou Formation, composed of andesite and basaltic andesite, and the Late Triassic Elashan Formation, consisting of basaltic tuff, dacite porphyry, and rhyolite porphyry. Additionally, the deposit is cross-cut by plutonic rocks that comprise a porphyritic granite with a granodioritic outer shell. The petrological characteristics, U-Pb ages, and cross-cutting relationships among these rocks are presented in Table 1. Ore bodies in Nageng are strictly fault-controlled and exhibit a steep dip of 70-85°, with EW-trending ore bodies occurring in the Jinshuikou Group and NE and NNW-trending ore bodies in the Elashan and Naocangjiangou Formations, respectively (Fig. 2a). The geometry of the ore bodies is commonly sigmoidal, with lengths ranging from 80 to 1560 m and thicknesses varying between 0.45 and 8.64 m (Fig. 2b; Xu et al., 2014; Guo, 2020). This deposit exhibits a distinct metal zonation extending from deep-level Pb-Zn mineralization to shallower Ag mineralization (Chen et al., 2022b).
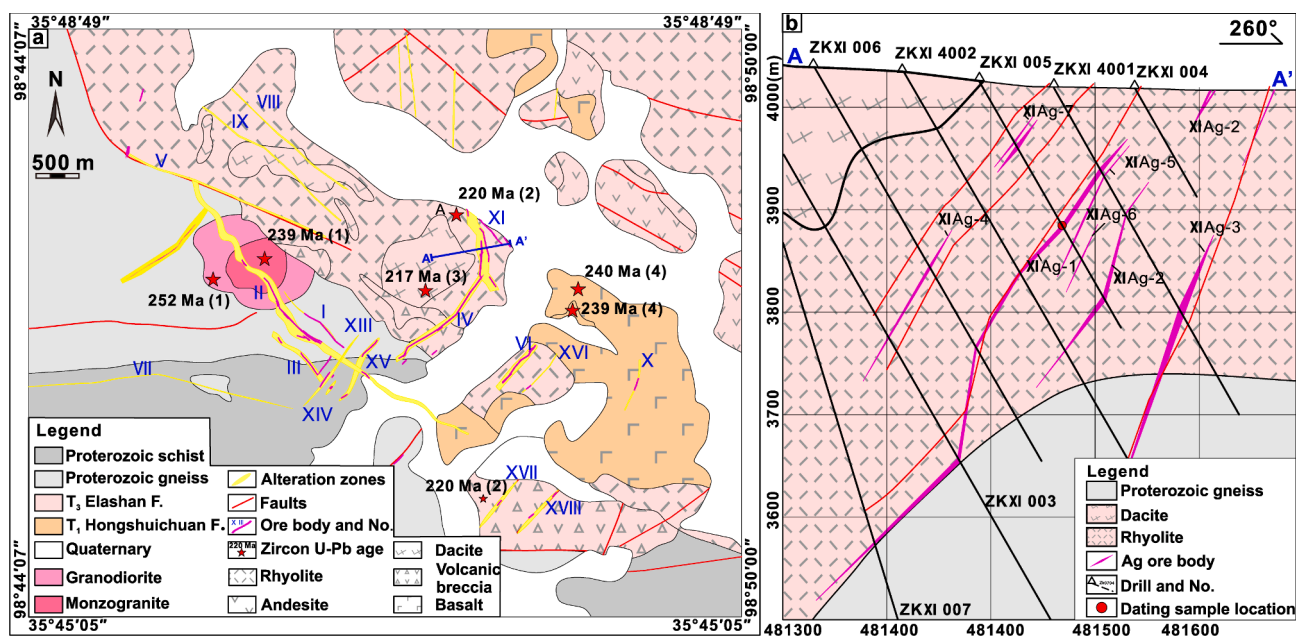

Fig. 2. (a) Geological map of the Nageng silver deposit showing the locations of the main silver ore bodies, and the profile A-A' (modified after Xu et al., 2020; Chen et al., 2021a). Ages labeled on the map are zircon U-Pb ages and the related references are listed in Table 1. (b) Representative cross-section in of the Nageng silver deposit (Modified after Chen et al., 2022b).

Table 1
A summary of the various rock types in the Nageng Ag-Pb-Zn deposit.

Rock types	Cross cutting relationship	Mineralogical characteristics	Age (Ma)	Reference
Monzogranite (1)	Cutting the Pt2 Jinshuikou G and cut by the ore body	Pl: 35–40%, Kfs:25–35%, Qz:25–30%, Bt:1–2%, and others	252 ± 1	Xu et al. (2020)
Granodiorite (2)	Cut by ore body and cutting monzogranite	Pl: 50–55%, Qz:20–25%, Bt: 5–8%, Hb: 5–8%, Kfs: 3–5% and others	239 ± 1	
Basaltic andesite (3)	Cutting by the ore body	Amp:10–15%, Pl, 35–40%, Px:<5% and others	240 ± 2	Chen et al. (2021)
Andesite (4)	Cutting the basaltic andesite	Amp:5–10%, Pl, 25–30%, Kfs:<5% and others	240 ± 2	
Basaltic tuff (5)	Cutting by the ore body and rhyolite	Phenocryst: Pl, 25–30%, Px: 3–5%, Qtz: 2%. Matrix: Pl, 45–50%, Px: 3–5%, tephros:10%	221 ± 2	Unpublished data
Dacite porphyry (6)	Host ore body and cutting the basaltic tuff	Pl: 25–35%, Hbl: 10–15%, others	220 ± 1	Chen et al. (2022b)
Rhyolite porphyry (7)	Host ore body and cutting the dacite porphyry	Qz: 30–35%, Pl: 25–35%, Kfs:5–10 %, others	217 ± 3	Guo et al. (2019)

Amp = Amphibole, Kfs = K-feldspar, Pl = Plagioclase Px = Pyroxene; Q z = Quartz, Hbl = Hornblende.

3.2. Hydrothermal alteration and paragenetic sequence

The Nageng silver deposit exhibits extensive hydrothermal alteration that diminishes with increasing distance from the mineralized veins. The dominant alteration minerals include quartz, sericite, and epidote, which demonstrate zoning patterns (Fig. 3h and i). As the alteration moves away from the ore body, the mineralization transitions from silicic to epidote and chlorite (Chen et al., 2019; Guo, 2020). Among them, the silicic alteration is closely connected to the silver mineralization and serves as a significant indicator for exploration efforts (Li and Li, 2017; Xu et al., 2020).

Based on the mineral paragenetic sequence and cross-cutting relationships (Figs. 3 and 4), three distinct stages of mineralization can be recognized in chronological order and these are three stages of mineralization followed by one post-ore stage.

(1) Stage 1 is characterized by weak sulfide mineralization (py1) and barren milky quartz (Fig. 3a, e), occurring as veinlets extending along strike within cracks or disseminations in wall rocks; (2) The subsequent stage 2 is characterized by the occurrence of abundant and massive sulfides (chalcopyrite, sphalerite, galena, pyrite (py2), marcasite, arsenopyrite, and pyrrhotite, Fig. 3f), in which sphalerite commonly bears chalcopyrite disease (Fig. 5d); (3) Stage 3 is marked by vein fault-fillings of extensional fractures that cut across stage 1 and 2 veins (Fig. 3b, c). The mineral assemblage in this stage is dominated by silver-bearing sulfosalts, accompanied by a relatively little sulfides (sphalerite, galena, pyrite (py3), marcasite, and pyrrhotite) and gangue minerals (quartz, calcite, and rhodochrosite, Fig. 3d, g). Sulfosalt species include freibergite, pyrargyrite, and stephanite, which commonly coexist with sphalerite and galena, replacing early-stage sulfides (Fig. 6); (4) Stage 4 is represented by post-ore veins, containing mainly calcite, quartz, and fluorite, and these are cross-cutting all previous stages (Fig. 4 a, b). The mineral paragenetic sequence is presented in Fig. 7.

3.3. Pyrite, sphalerite types and textures

Pyrite in the Nageng silver deposit has been grouped into three types based on their paragenetic stages. Py1 is present in stage 1 and is intergrown with barren quartz and rutile (Fig. 3e and 5a), which is characterized by euhedral crystals with sizes ranging from 10 to 300 μm (Fig. 5b). In some cases, visible sulfide inclusions occur along the rim (Fig. 5c). Py2 is commonly found in ores from stage 2 and appears in intergrowth with arsenopyrite, galena, and sphalerite (Fig. 5d). Py2 exhibits a subhedral-xenomorphic texture with crystal sizes ranging from 20 to 800 μm and has undergone metasomatism by conversion to marcasite and pyrrhotite, leading to the development of metasomatic relict textures (Fig. 5d) and locally undergone replacement by galena and arsenopyrite (Fig. 5e, f). Py3 is commonly found in ores of stage 3 and occurs as euhedral crystals with a size range of 20–400 μm (Fig. 5g), which are interspersed with early-formed marcasite (Fig. 5h, i).

The sphalerite occurrences within the Nageng deposit can be divided into two distinct types, differentiated by their textures and paragenetic stages. Sphalerite Type 1 (Sp1), primarily found at the stage 2, intergrowths with minerals including pyrite, marcasite, arsenopyrite, and galena (Fig. 3b and f), and is characterized by xenomorphic crystals ranging from 0.1 to 300 mm (Fig. 3b and 5b) and frequently containing chalcopyrite inclusions. sphalerite Type 2 (sp2), associated to the stage3, is intergrown with pyrite, calcite, and chalcopyrite, and is distinguished by euhedral crystals sized from 0.1 to 50 mm (Fig. 3g). It is replaced by stannite and pyrargyrite.

4. Sampling and analytical methods

Samples were acquired from various drill holes, and the specifics of each sample are condensed in Table 2. Petrographic examination was conducted on polished thin sections of every sample to effectively delineate the mineralogy, textures, and paragenesis.

4.1. Cathodoluminescence (CL) imaging

Prior to the analysis, the investigation of calcite internal textures by CL imaging was performed at the Institute of Geosciences and Geography, Martin Luther University Halle-Wittenberg, Halle (Saale), Germany. It was performed under a Zeiss A1 microscope coupled with CITL Cold Cathode Luminescence 8200 mk3. The high voltage ranges used in this experiment ranged from 20 kV to 25 kV, and the current ranges were from 200 μA to 250 μA.

4.2. The BSE and EPM analyzes

The EPMA was performed on a JEOL JXA-8230 electron microprobe at the Wuhan Sample Solution Analytical Technology Co., Ltd., Wuhan, China. The polished thin sections were carbon-coated before the analysis. Both the standards and samples were analyzed with a 5-μm spot diameter at a 15-kV accelerating voltage and a 20-nA beam current. The counting time was 20 s on peak and 10 s for the background on either side of the peak. Standards used for calibration include natural pyrite (for Fe and S), arsenopyrite (for As), chalcopyrite (for Cu), galena (for Pb), sphalerite (for Zn), pentlandite (for Ni), antimony telluride (for Sb) and native gold, silver and cobalt (for Au, Ag and Co, respectively). Images were acquired in BSE mode with an accelerating voltage of 15 kV and a primary beam current of 20nA.

4.3. LA-ICPMS u-pb dating of carbonate minerals

Calcite U-Pb dating was conducted using a Thermo Scientific quatraple iCap TQ inductively coupled plasma mass spectrometry (Q-ICP-MS) coupled with an ASI Resolution LR 193 nm ArF excimer laser ablation (LA) system at the Micro-Origin and Spectrum Laboratory (Sichuan Chuangyuan Weipu Analytical Technology Co. Ltd.), and
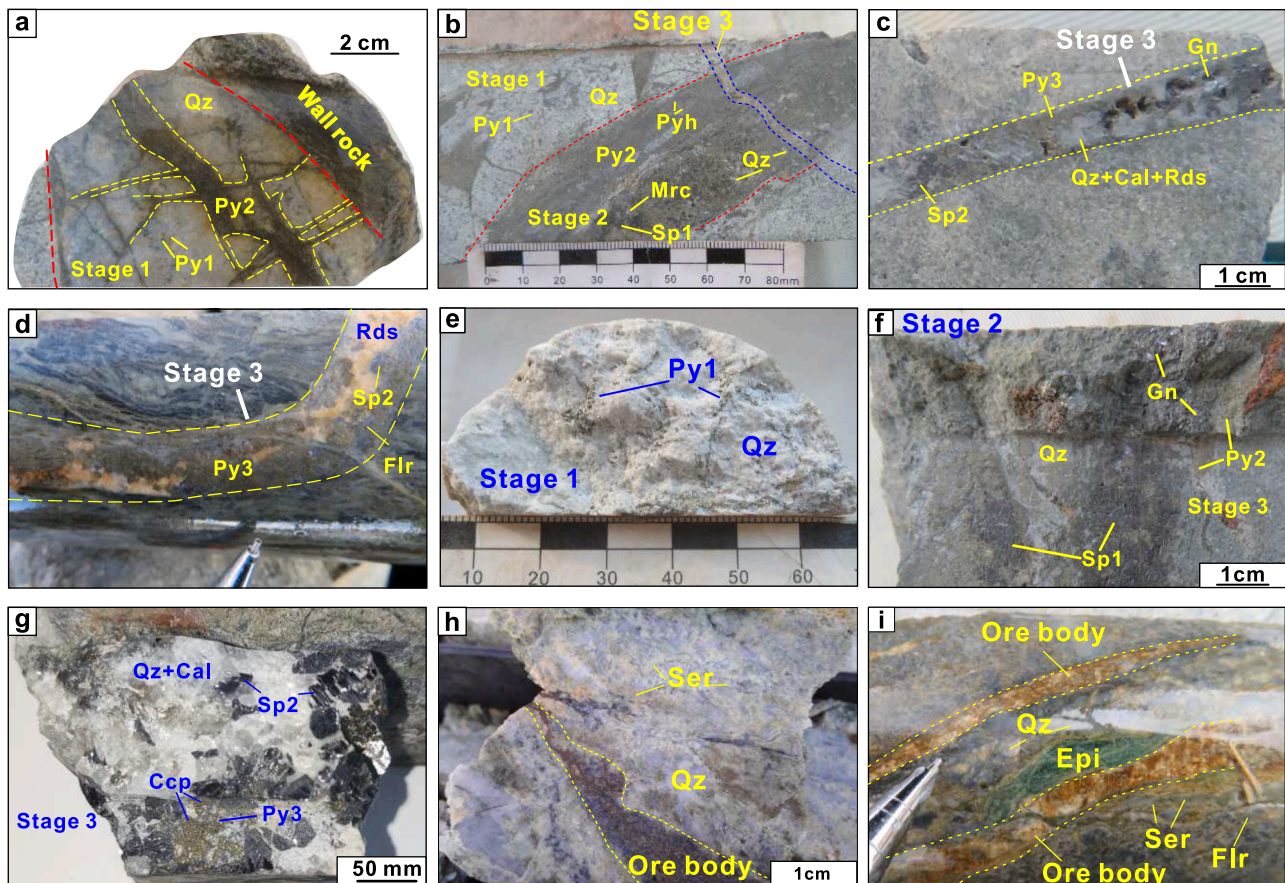
Fig. 3. Representative hand specimen photographs showing the cross-cutting relationship and mineral assemblages of different hydrothermal stages. (a) Stage 1 (milky barren quartz with pyrite) cut by stage 2. (b) Stage 2 massive pyrite, galena and sphalerite cut by stage 3. (c) and (d) The tensioned structure is filled with galena, sphalerite, calcite, quartz, and rhodochrosite. (e) Sparsely disseminated pyrite with milky quartz. (f) Massive sulfides with quartz. (g) Disseminated structure. (h) Phyllic zone. (i) Chloritization. (Apy = arsenopyrite; Gn = galena; Sph = sphalerite; Pyh = pyrrhotite; Py = pyrite; Ccp = chalcopyrite; Mrc = marcasite; Cal = calcite; Flr = fluorite; Qz = quartz; Rds = rhodochrosite; Ser = sericite; Epi = epidote; Stn = stannite; Rt = Rutile; Pyg = Pyrargyrite; =Fb = Freibergite). Abbreviations of minerals as per (Warr, 2021).

following standard methods described elsewhere (Roberts et al., 2017; Cheng et al., 2019; Shen et al., 2019; Luo et al., 2020; Nuriel et al., 2021). The corresponding instrument operating conditions and experimental parameters are summarized in Appendix A. ^{204}Pb was not measured due to the relatively high ^{204}Hg blank in the Ar-He carrier gas as well as in the calcite samples. In this experiment, PTKD yielded a U-Pb Tera-Wasserburg concordia lower intercept age of 154.0 ± 2.5 Ma (MSWD = 1.5), anchored using a ^{207}Pb/^{206}Pb value of value of 0.85 (Kendrick et al., 2022). The LD-5 calcite standard yielded a U-Pb Tera-Wasserburg concordia lower intercept age of 73.0 ± 0.55 Ma (MSWD = 1.5), also anchored using a ^{207}Pb/^{206}Pb value of 0.85.

4.4. Trace element analysis of pyrite

LA-ICP-MS analysis of pyrite trace element were conducted using an Agilent 7700e ICP-MS spectrometer coupled with Coherent 193 nm excimer laser, at the Wuhan Sample Solution Analytical Technology Co., Ltd., Wuhan, China. Detailed operating conditions for the laser ablation system and the ICP-MS instrument and data reduction are the same as description by (Zong et al., 2017). The ablated patches were 32 μm in size. Measurements at each point included 20–30 s of instrument background and 50 s of sample ablation. Trace element compositions of sulfides were calibrated against various reference materials NIST 610 without using an internal standard (Liu et al., 2008). The sulfide reference material of MASS-1 (Wilson et al., 2002) (USGS) was used as the unknown sample to verify the accuracy of the calibration method. The

Excel-based software IOLITE (Paton et al., 2011) was used for data calculation.

4.5. In-situ sulfur isotopic analysis of pyrite and sphalerite

In-situ sulfur isotope analyses were performed using a Neptune Plus MC-ICP-MS, equipped with a RESOlution SE 193 nm laser ablation system at the Beijing Createch Testing Technology Co., Ltd, China. The laser beam diameter was 50 μm with a laser repetition rate of 8 Hz and the ablation time span was 27 s. Standard-sample bracketing (SSB) was used to determine δ^{34}S values of samples throughout the MC-ICP-MS analysis. The true sulfur isotopic ratios were calculated by correcting for instrumental mass bias via linear interpolation between the biases calculated from two neighboring standard analyses. Isotopic data were reported in delta notation (‰) relative to Vienna-Canyon Diablo Troilite (V-CDT). The analytical precision (1σ) was determined to be approximately ± 0.1‰ (Bendall et al., 2006; Mason et al., 2006).

5. Results

5.1. U-pb data of calcite

In total, 100 LA-ICP-MS spot analyses were performed on a post-ore calcite sample. The ^{238}U/^{206}Pb ratios ranged from 0.03 to 21.70, and the ^{207}Pb/^{206}Pb ratios ranged from 0.269 to 0.848 (Suppl Table. S1), revealing a lower intercept age of 207 ± 3 Ma with an initial
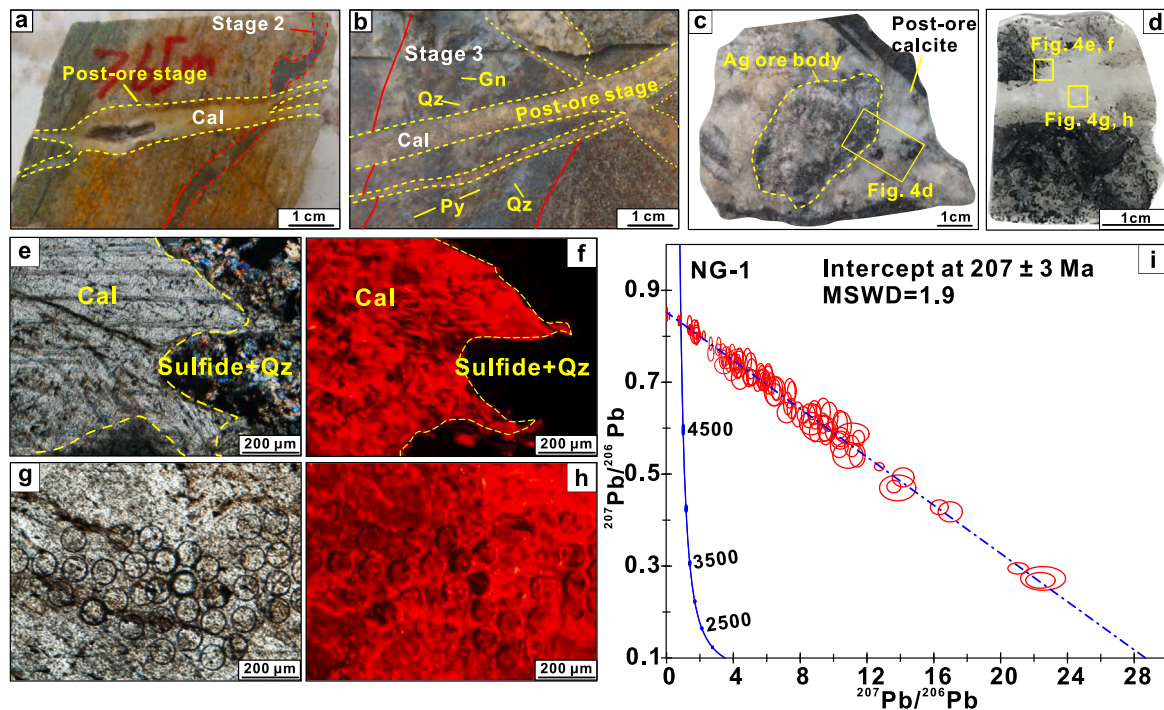
Fig. 4. Representative images of Ag ore bodies and post-ore calcite veins. (a-c) Hand specimen images showing the Ag ore body cut by post-ore calcite veins. (d) Thin section image of the same sample. Photomicrographs of a post-ore calcite vein under (e) plane-polarized light and (f) cathodoluminescence (CL) imaging. Photomicrographs of the location of LA-ICP-MS spot analyzes under (g) plane-polarized light and (h) CL imaging. (i) Tera-Wasserburg concordia diagram of LA-ICP-MS U-Pb data of a late-stage calcite vein. Error ellipses represent 2σ. MSWD denotes the mean standard weighted deviation. The meaning of the mineral's abbreviations was list in the caption of the Fig. 3.

^{207}Pb/^{206}Pb value of 0.851 and a mean square weighted deviation (MSWD) of 1.9 in the Tera-Wasserburg diagram (Fig. 4i).

5.2. Chemical compositions of silver and silver-bearing minerals

EPM analyses were carried out at the Nageng silver deposit to identify several Ag minerals, as well as galena and sphalerite. The results of these analyses can be found in Supple Table S2.

Pyrargyrite (Ag_3SbS_3) is the most common Ag mineral in the Nageng deposit. It has a consistent chemical composition of Ag (59.45–60.70 wt %), Sb (20.66–21.80 wt%), and S (16.85–17.83 wt%), with low levels of Zn, Fe, Cu, and Pb.

Freibergite ((Ag, Cu)$_{10}$(Fe, Zn)$_2$(Sb, As)$_4S_{13}$) is the second most common Ag mineral. It primarily consists of Ag (26.80–33.86 wt%), Sb (20.65–25.13 wt%), and S (20.39–22.85 wt%). It has higher concentrations of Cu (13.80–18.28 wt%) and Fe (5.22–10.22 wt%) than other silver-bearing minerals, and low levels of Zn and Pb.

Stephanite (Ag_5SbS_4) is a rare mineral in the deposit. It has the highest Ag (64.73–69.56 wt%), Sb (14.04–19.41 wt%), and S (15.00–15.56 wt%) contents, with low levels of Zn, Fe, Cu, and Cd.

Galena (PbS) has low S content (13.52–13.90 wt%) and high Pb content (84.30–86.43 wt%), with varying levels of Ag (0.01–0.92 wt%) and Sb (0.02–0.81 wt%). The contents of Fe, Cu, Zn, Co, and Ni are low. The Ag/Pb ratios for galena vary from 0.0001 to 0.0109, and there is a linear correlation between the mole proportion of Ag, Sb, and Ag + Sb in galena and that of Pb.

Sphalerite (ZnS) has high Zn content (47.78–53.72 wt%), high S content (33.06–34.37 wt%), and Fe content (12.05–14.58%). The contents of Pb, Cu, Sb, Ag, Au, As, Zn, Co, and Ni are mostly below the detectable limits. The total content analysis indicated that sp2 had a concentration of 96–97%. However, the EDS analysis showed a significant peak of Mn element in sp2 that was not tested in the electron probe analysis. As a result, it is plausible to assume that sp2 has a higher Mn content compared to sp1.

5.3. Pyrite trace element contents

In total, 55 LA-ICP-MS spot analyses were conducted on pyrite samples, revealing concentrations of Mn, Co, Ni, Cu, Zn, As, Ag, Sn, Sb, Pb, and Bi above the detection limits. Conversely, concentrations of Ca, V, Cr, Ga, Mo, Cd, In, W, Pt, and Au were either close to or below the detection limits (Supple Table S3). The resulting data are presented in Figs. 8 and 9. Compared to the other generations of pyrite, py1 has higher concentrations of arsenic (medium 701 ppm), Zn (medium 21.0 ppm), Cu (medium 8.1 ppm), Co (medium 3.6 ppm), Sn (medium 49.9 ppm) and Mn (medium 56.8 ppm). The Co/Ni value ranges from 0.3 to 6.1 (medium 1.4 ppm). Py2 contains Bi (medium 1.1 ppm) and Pb (medium 80.5 ppm), while most of the Co contents are below the detection limit. Py3 preserves the highest Ni content (medium 25.3 ppm), Sb (medium 30.0 ppm) and the Co/Ni value ranges from 0.01 to 0.04 (medium 0.02 ppm).

5.4. In-situ analyses of sulfur isotope compositions

In this study, we performed a total of 34 LA-ICP-MS spot analyzes to determine the sulfur isotopic compositions of pyrite and sphalerite samples from the Nageng silver deposit (py1 = 8, py2 = 11, py3 = 6, sp1 = 7, and sp2 = 2). The resulting data are presented in Table 3 and depicted in Fig. 10. Overall, the pyrite samples exhibit a relatively uniform δ^{34}S value, ranging from −2.59 to + 2.05 ‰ with an average of −0.74 ‰ (Fig. 10a). In addition, each type of pyrite displays a distinctive δ^{34}S signature. Py1 has a range of −1.34 ‰ to 2.05 ‰, py2 ranges from −2.59 ‰ to 0.43 ‰, and py3 ranges from −0.77 ‰ to 0.78 ‰. In contrast, sphalerite shows a wider range of sulfur isotopic compositions, varying from −4.23 to −0.05 ‰ (Fig. 10b). The δ^{34}S values of sp1 range from −4.23 to −1.96 ‰, and sp2 range from −0.48 to −0.05 ‰.
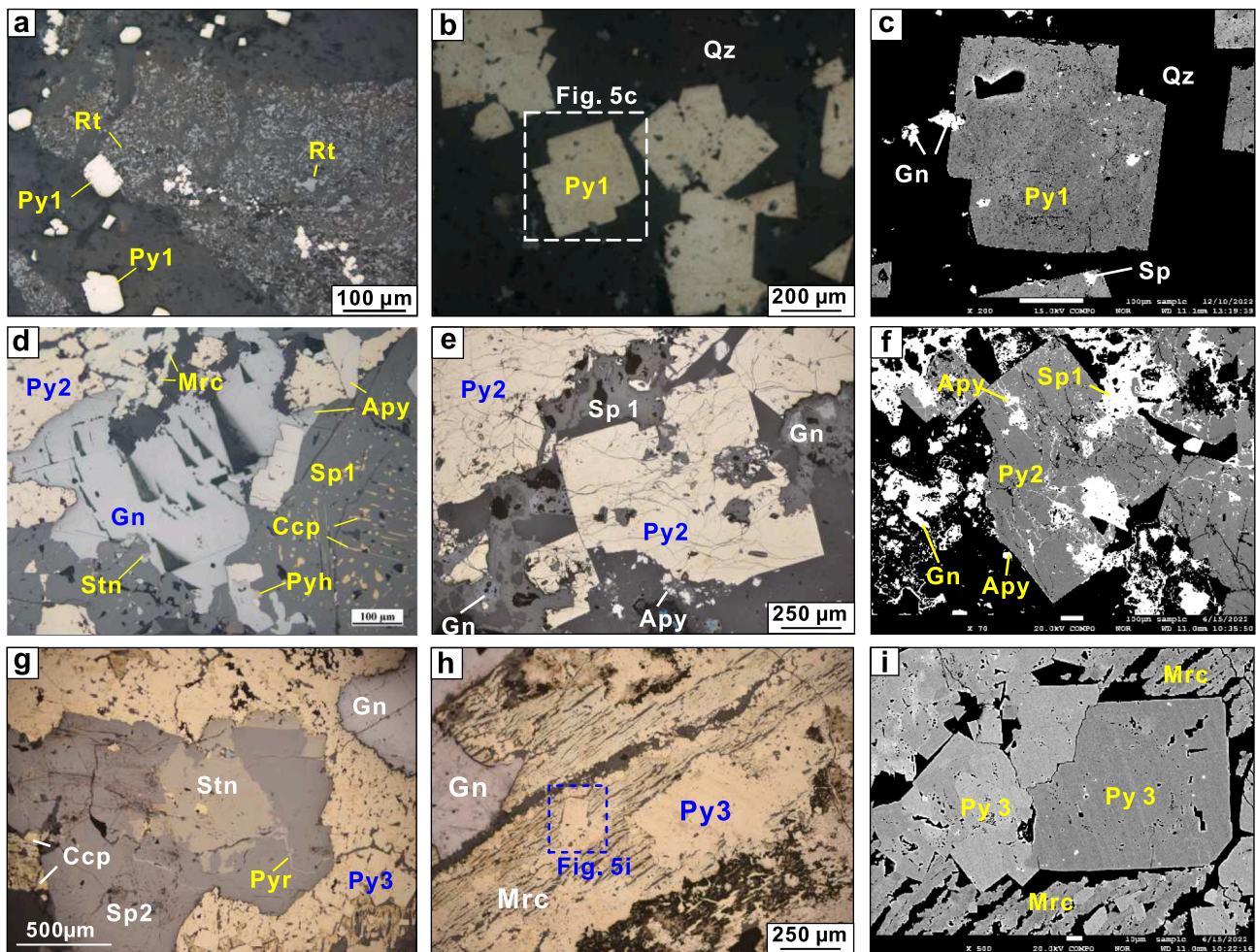
Fig. 5. Representative photographs showing the mineral assemblages, texture, and paragenesis of pyrite and sphalerite from different hydrothermal stages. (a) Pyrite (py1) coexisting with quartz and rutile (stage 1). (b, c) Medium-grained pyrite with euhedral shape (py1) association with minor galena and sphalerite. (d) Py2 grains coexist with abundant galena, sphalerite (sp1) commonly bears chalcopyrite disease, marcasite, and arsenic pyrite (stage 2). (e, f) Subhedral-xenomorphic pyrite (py2) replaced by galena and sphalerite. (g) Euhedral crystals of pyrite (py3) intergrown with galena, chalcopyrite, sphalerite (sp2), stannite, and pyrargyrite (stage 3). (h, i) Early-formed marcasite was interspersed by euhedral crystals pyrite (py3). The meaning of the mineral's abbreviations was list in the caption of the Fig. 3.

6. Discussion

6.1. Mineralization age

The mineralization age of the Nageng silver deposit is challenging to determine directly due to the absence of suitable geochronometers. Consequently, the spatial relationship between ore bodies and the surrounding wall rocks becomes crucial in establishing the timing of silver mineralization. The Nageng silver deposit is situated within the Jinshuikou Group and the Elashan Formation (Fig. 2a). The Jinshuikou Group (2.2–1.8 Ga) mainly comprises amphibolite- to granulite-facies metamorphic paragneiss and schist (Guo, 2020; Xu et al., 2020). The Elashan Formation in the Nageng district has various types of volcanic rock (Table. 1). Among them, the youngest age is derived from a rhyolitic porphyry with a zircon U-Pb age of 217 ± 3 Ma (Guo et al., 2019). Field and microscopic observations indicate that ore bodies directly cut across the rhyolites (Fig. 3a, b, and c), while the wall rocks underwent widespread alteration due to interaction with the hydrothermal fluids (Fig. 3h, i). Furthermore, as shown in Supple Figure S2, Pb isotopic compositions of the Elashan Formation show a scattered distribution. In contrast, sulfides from Nageng demonstrate a narrow range of Pb isotopic compositions compared to the Elashan Formation volcanic rocks. This most likely suggests that the contribution of volcanic rocks in respect to the silver mineralization is limited. Therefore, the timing of

the silver mineralization in the Nageng deposit postdates the volcanic eruptions. The age (ca. 217 Ma) of the rhyolitic porphyry can thus define the maximum age of the silver mineralization. Moreover, according to field and macroscopic observations, the later stage calcite is identified (Fig. 4 a, b), yielding a LA-ICP-MS U-Pb age (207 ± 3 Ma) for calcite, which provides the minimum age for the silver mineralization. To sum up, the mineralization time of the Nageng deposit can be constrained between ca. 217–207 Ma.

The temporal occurrence of the Nageng Ag deposit aligns with ages recorded for other deposits within the EKOB, including the Saishentang Skarn Cu-Mo-Sn deposit (molybdenite Re-Os: 223.4 ± 1.5 Ma; Wang et al., 2016), the Kendekeke Skarn Fe deposit (Sericite $^{40}Ar/^{39}Ar$: 222.4 ± 2.5 Ma; Xiao et al., 2013), the Changshan and the Halongxiuma porphyry Mo deposit (molybdenite Re-Os ages ranging between ca. 214–223 Ma; Feng et al., 2010; Lu et al., 2017). This correspondence implies a significant regional stage of mineralization in the EKOB during the Late Triassic.

6.2. Source of metals and sulfur

Based on field and micrographic analysis, the primary constituents of the Nageng silver deposit were identified as sulfide minerals, and together with the absence of sulfate minerals and hematite suggests reducing conditions (Ohmoto, 1972; Börner et al., 2022). Additionally,
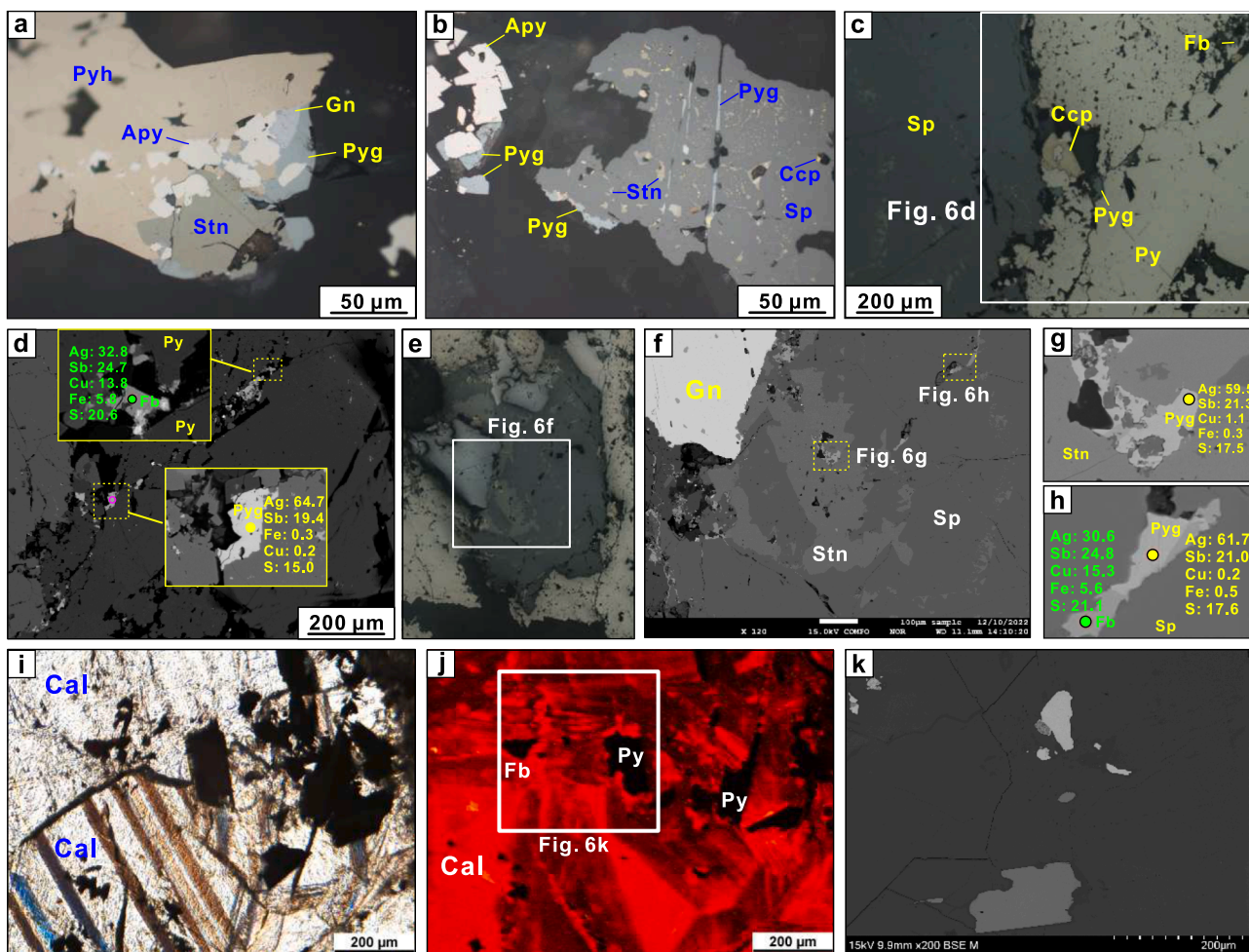
Fig. 6. (a) Pyrargyrite in interstices between arsenopyrite, pyrrhotite, galena, and stannite. (b) Pyrargyrite dissemination in sphalerite. (c-d) Silver minerals dissemination in pyrite. (e-h) Fine pyrargyrite and freibergite inclusions in sphalerite. (i–k) Intergrowth of calcite with silver minerals. The meaning of the mineral's abbreviations was list in the caption of the Fig. 3.

Stages / Minerals	Ore forming stages			Post-ore stage
	Stage 1	Stage 2	Stage 3	
Ore minerals in vein				
Pyrite	Py1	Py2	Py3	
Arsenopyrite				
Chalcopyrite				
Galena				
Sphalerite		Sph1	Sph2	
Pyrrhotite				
Marcasite				
Stannite				
Tetrahedrite				
Pyrargyrite				
Jamesonite				
Freibergite				
Native silver				
Rutile				
Alteration and gangue				
Quartz				
Calcite				
Sericite				Calcite U-Pb dating
Fluorite				
Rhodochrosite				

– – – – – Rare ———— Minor ▬▬▬▬ Major

Fig. 7. Mineral paragenesis and assemblage diagram of the Nageng Ag deposit.

Table 2
Locations and descriptions of samples used for this study.

Sample No.	Drill No.	Level (m)	Stage	Ore minerals		Gangue minerals	Analyses
				Major	Minor		
7	ZK2304-2	561 m	Stage 1	Py	Apy, Sph, Gn	Qz	BSE, LA-ICP-MS
19	ZK1602-2	933 m	Stage 1	Py	Apy, Sph, Gn	Qz	BSE, LA-ICP-MS
16	ZK0705-8	900 m	Stage 2	Sph, Gn, Apy	Ccp, Po, Mrc	Qz	BSE, LA-ICP-MS
20	ZK1602-4	49 m	Stage 2	Py, Apy	Ccp, Po, Mrc	Qz	BSE, LA-ICP-MS
24	ZK0704-1	424 m	Stage 2	Sph, Gn, Py	Po, Mrc	Qz	BSE, EMP
32	ZK0707-5	649.5 m	Stage 2	Sph, Gn, Py	Mrc, Po	Qz	BSE
34	ZK0707-6	646 m	Stage 2	Sph, Gn, Py	Mrc	Qz	BSE,
39	ZK0707-10	590 m	Stage 3	Py, Sph, Apy	Gn, Ccp, Stn	Qz, Cal	BSE, EMP,
40	ZK0707-10	643 m	Stage 3	Sph, Py, Apy	Gn, Ccp, Mrc	Qz, Cal	BSE,
45	ZK0707-12	590 m	Stage 3	Sph, Py, Gn	Ccp, Mrc	Qz, Cal	BSE, LA-ICP-MS
43	ZK0707-11	627 m	Stage 3	Sph, Py, Gn	Ccp, Mrc	Qz, Cal, Rds	BSE, EMP
46	ZK0707-12	590 m	Stage 3	Sph, Py, Gn	Ccp, Mrc	Qz, Cal, Rds	BSE, LA-ICP-MS
ZST1	ZKXI005	600 m	Ore body	Py	Sph, Gn	Qz, Cal	Calcite U-Pb, CL
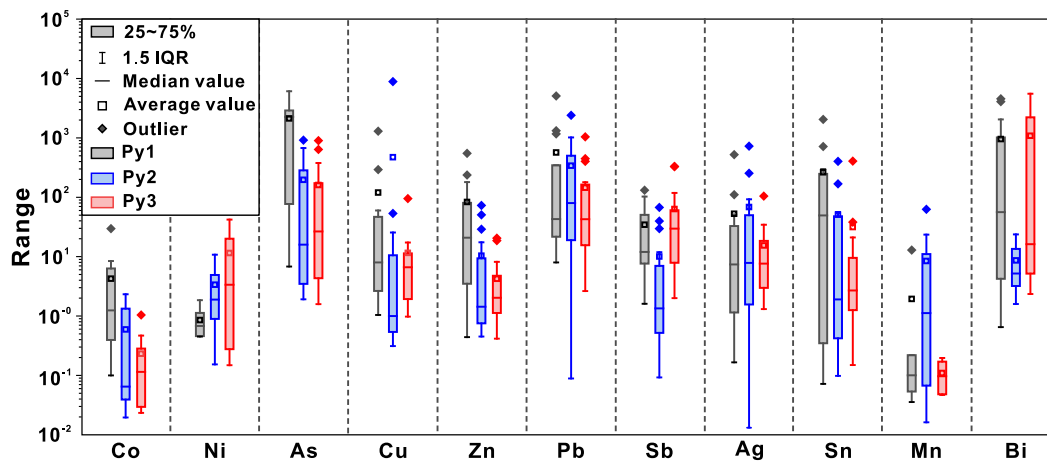
Fig. 8. Box-and-whisker plots of trace element compositions of pyrite from the Nageng deposit.

the relationship between the sulfur isotopic compositions of the various sulfides in Nageng is expressed as galena (avg. −3.07 ‰) < sphalerite (avg. −1.59 ‰) < pyrite (avg. −0.94 ‰) (Fig. 10a; Chen et al., 2019; Xu et al., 2020; Cheng, 2022), indicating that these sulfides attained sulfur isotopic equilibrium during their formation (Ohmoto and Rye, 1979). Generally, when sulfides precipitate in a hydrothermally reducing and equilibrating mineralizing environment, the $\delta^{34}S$ values of sulfides values are roughly equal to the total $\delta^{34}S$ values of ore-forming fluids (Ohmoto, 1972; Ohmoto and Rye, 1979).

The bulk pyrite $\delta^{34}S$ values (−4.00 to + 3.90 ‰; Chen et al., 2019; Xu et al., 2020) have a broader range than the in-situ analyses of pyrite (-2.59 to + 2.05 ‰). Notably, though the presence of inclusions can introduce influences in both bulk and in-situ analyses, the latter approach offers enhanced discrimination among discrete pyrite populations and their associated $\delta^{34}S$ signatures (Wang et al., 2021a; Grema et al., 2022; Martin et al., 2023). The in-situ sulfur isotopic compositions of hydrothermal fluids from stage 1 to stage 3 exhibit relative homogeneity and align with the isotopic composition range of the magmatic sources (0 to ± 5.0 ‰; Ohmoto and Rye, 1979). Additionally, bulk $\delta^{34}S$ values in Nageng silver deposit (−4.0 to + 3.90 ‰) are in the neighborhood of sulfur isotopic compositions for sulfides of nearby magmatic-hypothermal deposits with heterogeneous $\delta^{34}S$ values of −5 to + 5 ‰ (Fig. 8 c; Fan et al., 2021; Liang et al., 2021; Wu et al., 2021; Li et al., 2021b; Zhao et al., 2021b; Cong et al., 2023). Previous studies have suggested that the late-stage mineralization system was influenced by the input of meteoric water, as indicated by the C-H-O isotopes in the coexisting quartz (Li and Li, 2017; Chen et al., 2019). However, despite some isotopic variation between the early and late stages, the $\delta^{34}S$ values of the Py3 formed during stage 3 remained relatively constant

(Fig. 10b), suggesting limited interaction with meteoric water during the silver mineralization stage. Additionally, the $^{206}Pb/^{204}Pb$, $^{207}Pb/^{204}Pb$, and $^{208}Pb/^{204}Pb$ ratios for the Nageng ore minerals are very similar to those of magmatic-hydrothermal ore deposits in the EKOB (Supple Fig. S2a, b), suggesting that the Nageng ores and these deposits shared a common source for their metals, which is the result of the interoperation of the mixing magmatism of the upper crust and mantle (Fan et al., 2021; Liang et al., 2021).

6.3. Trace elements of pyrite provide clues to the metallogenetic processes

6.3.1. Trace element distribution in pyrite

Trace elements in pyrite predominantly exist as structurally bound solid solutions (Huston et al., 1995; Reich et al., 2013) and micro- to nano-sized mineral inclusions (Deditius et al., 2011; Kouhestani et al., 2017; Sykora et al., 2018). Understanding the distribution of these trace elements in pyrite is essential for the interpretation of the mineralization processes (Elatikpo et al., 2022; Zhu et al., 2022). The LA-ICP-MS time-resolved depth profiles of Co, Ni, and As are smooth and consistent with Fe (Supple Fig. S1). This indicates that Ni and Co replace Fe, while As replaces S through isomorphous substitution in the pyrite lattice. Lead (Pb) has a larger ionic radius than Fe^{2+} and therefore, it is unlikely to enter the pyrite crystal lattice. It also has a faster precipitation rate than pyrite (Shannon, 1976; Morse and Luther, 1999), leading to its common occurrence as micro- or nano-inclusions in pyrite (Reich et al., 2013; Keith et al., 2016). Additionally, it may also occur as a structurally bound element or in nanometer-sized inclusions that are not always detected by LA-ICP-MS, as shown by a flat Pb profile (Supplement Fig. S1; Román et al., 2019; Wang et al., 2021b). The concentrations of
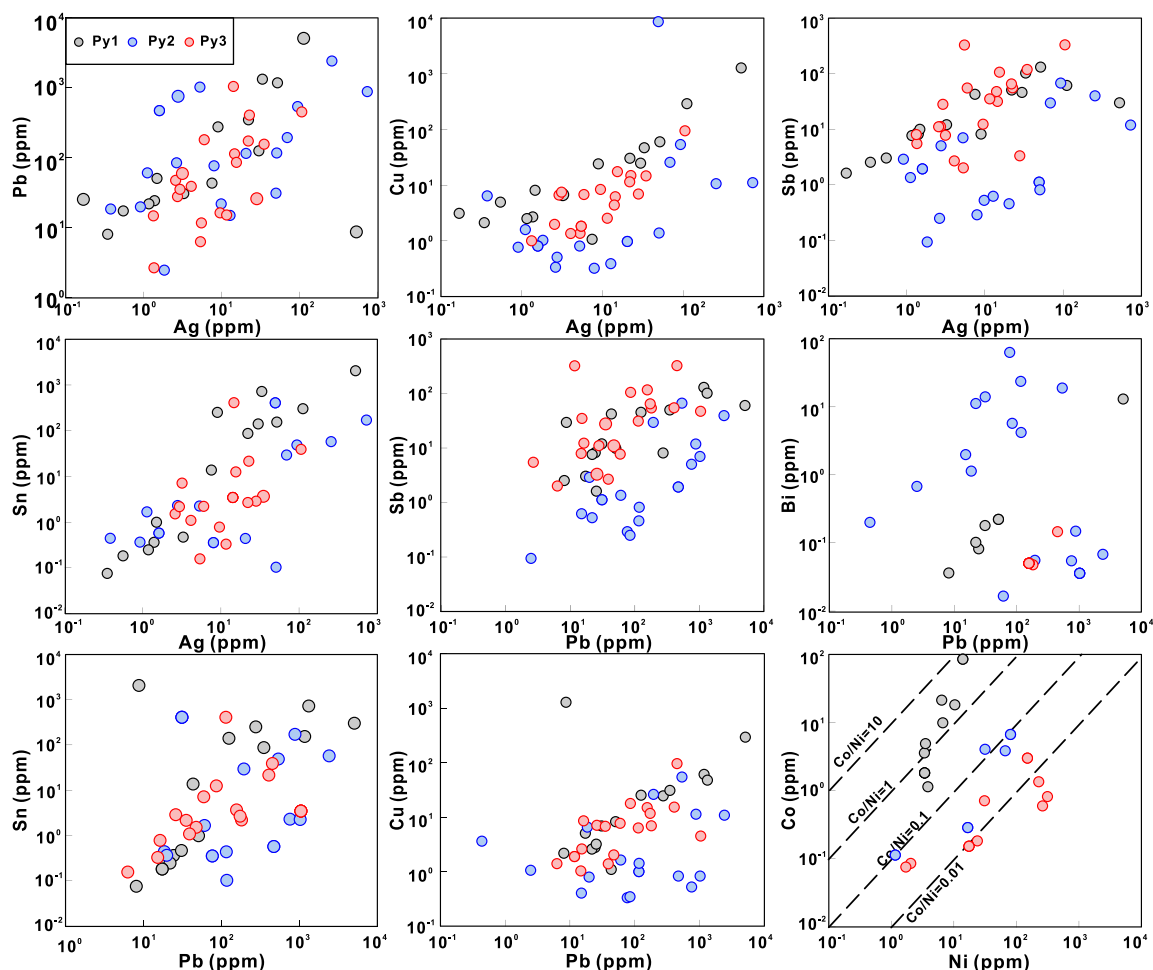
Fig. 9. Binary plots of trace elements in pyrite from different mineralization stages (a) Pb vs. Ag, (b) Cu vs. Ag, (c) Sb vs. Ag, (d) Sn vs. Ag, (e) Sb vs. Pb, (f) Bi vs. Pb, (g) Sn vs. Pb, and (h) Co vs. Ni. Trace element concentrations listed in Supple Tab. S3. All measurements below minimum detection limits are discarded.

Mn (0.66 to 5536 ppm), Sn (0.07 to 2052 ppm), Cu (0.32 to 8891 ppm), and Zn (0.42 to 553 ppm) in pyrite exhibit significant variability of these elements. Furthermore, multiple spikes and chaotic denudation signals in the LA-ICP-MS time-resolved depth profiles of all three types of pyrite (Supple. Fig. S1) indicate that Mn-compounds, stannite, chalcopyrite, and sphalerite occur as micro- to nano-mineral inclusions in pyrite.

Depth profiles of pyrite typically exhibit coupled peaks of Ag, Cu, Sb, Sn, and Bi (Supple. Fig. S1), which are commonly accompanied by positive correlations among these elements (Fig. 9A–h). This may represent that Ag is hosted in galena by coupled ion substitution, such as $Ag^+ + (Sb, Bi)^{3+} \leftrightarrow 2Pb^{2+}$, or $(Ag, Sn, Cu)^+ + (Sb, Bi)^{3+} \leftrightarrow 2Pb^{2+}$ (Renock and Becker, 2011; Gregory et al., 2015; Keith et al., 2020; Wang et al., 2021b). In certain depth profiles, Ag, Cu, Sn, and Sb curves in the signal diagrams may exceed and diverge from the lead curves (Supple. Fig. S1). This divergence can indicate the potential existence of Ag-bearing sulfosalt inclusions in pyrite, including pyrargyrite, freibergite, and stephanite.

6.3.2. Evolution of the ore-forming fluids and conditions of silver ore formation

Pyrite is a common mineral in various types of mineral deposits, and its precipitation is influenced by factors such as temperature, pH, fO_2, and fS_2, which contribute to variations in pyrite compositions and the paragenetic sequence (Huston et al., 1995; Maslennikov et al., 2009; Wang et al., 2019; Li et al., 2023a). In the Nageng silver deposit, distinct pyrite textures, trace element compositions, and irregular in-situ $\delta^{34}S$ values of sulfides indicate temporal variations in the fluids responsible

for ore formation.

Petrography and trace element data in py1 suggest that fluids in the earliest mineralization stage of the Nageng silver deposit were enriched in As, Cu, Pb, Zn, Ag, Sn, Sb, and Mn (Fig. 8). The Co/Ni ratio of > 1 suggest that py1 likely is hydrothermal pyrite (Fig. 9i; Clark et al., 2004; Rudnick and Gao, 2014; Liang et al., 2021). Py1 exhibits relatively low concentrations of Co (medium 3.6 ppm) and Ni (medium 5.1 ppm), which are within the typical range for felsic magmatic rocks (Co < 8 ppm, Ni < 27 ppm; Rudnick and Gao, 2014). Moreover, the previously published Pb isotopic compositions of sulfides in the Nageng silver deposit are close to that of granitic porphyry rocks, which are revealed by data from a drill hole sunk at the Nageng silver deposit (Supple Fig. S2; Chen et al., 2021a). Therefore, it is likely that py1 originated from felsic magmatic-hydrothermal fluids enriched in an association of As-Cu-Pb-Zn-Ag-Sn-Sb.

Py2 exhibits lower concentrations of trace elements and $\delta^{34}S$ values compared to py1. Previous studies have indicated that the substitution of Co for Fe in pyrite is more likely to occur at higher temperatures (Clark et al., 2004; Grant et al., 2018; Román et al., 2019). The lower Co content in py2, mostly below the detection limit, compared to py1 (with a median value of 3.6 ppm), suggests a temperature decrease from stage 1 to stage 2. This observation aligns with micro-thermometric data obtained from co-existing quartz, which also indicates a temperature decrease from stage 1 (270–330 °C) to stage 2 (250–310 °C), within the NaCl equivalent range of 4 to 7 wt% (Chen et al., 2019). A temperature decrease can lead to sulfide precipitation, resulting in S isotope fractionation with lighter isotopes being incorporated into subsequently

Table 3
LA-MC-ICPMS in-situ sulfur isotopic compositions for different generations of pyrite and sphalerite in the Nageng Ag-Pb-Zn deposit.

Sample. No	Sulfide generation	δ^{34}S (V-CDT) (‰)
19-Py-1	Py1	2.05
19-Py-2	Py1	0.22
19-Py-3	Py1	1.05
7-Py-1	Py1	−0.64
7-Py-2	Py1	−0.04
7-Py-3	Py1	−0.44
7-Py-4	Py1	−0.89
7-Py-5	Py1	−1.34
20-Py-1	Py2	−0.54
20-Py-2	Py2	0.43
20-Py-3	Py2	−0.92
16-Py-1	Py2	−1.64
16-py-2	Py2	−2.57
16-py-3	Py2	−2.59
32-Py-1	Py2	−1.98
32-Py-1	Py2	−2.42
32-Py-2	Py2	−2.44
32-Py-3	Py2	−2.03
32-Py-4	Py2	−1.71
45-Py-1	Py3	0.78
45-Py-2	Py3	0.45
45-Py-3	Py3	−0.38
40-Py-4	Py3	−0.47
40-Py-5	Py3	0.34
45-Py-6	Py3	−0.77
32-Sp-1	Sp1	−1.96
32-Sp-2	Sp1	−2.65
32-Sp-3	Sp1	−4.23
32-Sp-4	Sp1	−3.08
34-Sp-1	Sp1	−3.00
34-Sp-2	Sp1	−2.80
34-Sp-3	Sp1	−2.77
7-Sp-1	Sp1	−3.33
7-Sp-2	Sp1	−3.24
45-Sp-1	Sp2	−0.05
45-Sp-2	Sp2	−0.48

formed sulfides. This reduction in fS$_2$ in fluids can consequently lead to lower δ^{34}S values in pyrite (Pokrovski et al., 2019). Elements consumed during the formation of arsenopyrite, galena, and sphalerite, such as, Pb, Zn, Cu, and Sb, can cause lower concentrations of these elements in py2 compared to py1 (Fig. 8). Furthermore, during the formation of galena in stage 2, Ag, Sb, as well as Bi were homogeneously incorporated.

Based on thermodynamic calculations of freibergite (Sack, 2005), the temperature range for the primary silver mineralization in stage 3 is estimated to be 170–300 °C, with the majority of values falling between 180 and 220 °C (Fig. 11a). This suggests that stage 3 is formed under relatively low-temperature conditions compared with stages 1 and 2. This conclusion is further supported by the decrease in the average Fe contents in sphalerite, which is positively correlated with mineralization temperature (Keith et al., 2014; Han et al., 2022), from 13.25 wt% in stage 2 (sp1) to 12.13 wt% in stage 3 (sp2). In addition, the mineral assemblages and temperature data (Fig. 12b), suggest that the Nageng ore assemblage belongs to the intermediate-low sulfidation field. The ore deposition in the Nageng veins began at moderate fS$_2$ conditions (-6 to −8), within the stability fields of pyrite at approximately 300 °C for the stage1, and slowly decreased to fields of pyrite and arsenopyrite at approximately 280 °C for stage 2. The deposition then progressively evolved to a lower fS$_2$ state (-14 to −18), coeval with the deposition of silver sulfosalts, such as freibergite and pyrargyrite, within the fields of the freibergite-pyrargyrite-pyrrhotite assemblage at around 220 °C for the Ag-sulfosalt formation. Additionally, the presence of stage 3 in a fracture-filled vein (Fig. 7) indicates low pressure conditions during its formation compared to stage 1 and 2. Previous study has established that a decrease in temperature, pressure, and fS$_2$ can lead to a decrease in the δ^{34}S values of pyrite (Ohmoto and Rye, 1979). However, the increase in δ^{34}S values of py2 to py3, and sp1 to sp2 (Fig. 10b) suggest that

additional factors may have influenced the alteration of the S isotopic composition of pyrite in stage 3.

The intergrowth of Ag sulfosalt and calcite (Fig. 6i-k) in stage 3 provides valuable evidence of a decrease in fO$_2$ (Zhai et al., 2018; Zhai et al., 2020). Multiple lines of evidence support this decrease in fO$_2$. Firstly, py3 exhibits higher Ni contents (median 25 ppm) compared to py1 and py2, as Ni is known to preferentially substitute for Fe in pyrite under low fO$_2$ conditions (Lehner et al., 2006; Savage et al., 2008). Moreover, sp2 in stage 3 has high Mn contents compared with sp1 in stage2, which is generally indicative of a relatively reduced environment (Kelley et al., 2004; Zhao et al., 2022). A decrease in fO$_2$ of the ore-forming fluids can result in ^{34}S enrichment in later-formed sulfides, leading to slightly negative or positive δ^{34}S values of pyrite (Ward et al., 2017; Yue et al., 2021; Li et al., 2023a; Shan et al., 2023).

Above of all, stage 3 is proposed to have formed in a low fO2 environment compared with stages 1 and 2. The prevalence of silica and sericite as the dominant hypothermal alteration minerals, coupled with the lack of kaolinite and K-feldspar, implies formation under near-neutral conditions (Li et al., 2019; Zhai et al., 2019). Under near-neutral conditions it is plausible to interpret the transport of silver in silver bisulfide-complexes (Seward, 1976; Gammons and Barnes, 1989; Williams-Jones et al., 2014). As temperature, fS2, and fO2 decrease dramatically in stage 3, the system transitions to a lower fS2 and fO2 state with near-neutral pH, resulting in the precipitation of silver sulfosalts along with calcite (Li et al., 2019; Zhai et al., 2019; Zhai et al., 2020).

### 6.4. Implication for ore genesis

Based on the synthesis of geological, geochronological, mineralogical, and geochemical data, a genetic model explaining the genesis of the Nageng Ag deposit is depicted in Fig. 12. The in-situ sulfur isotope analyzed in this study, along with prior research on sulfide Pb and co-existing quartz C-H-O isotopic systematics, confirms the deep magmatic metal and sulfur source of the Nageng deposit (Chen et al., 2019; Xu et al., 2020). The Nageng deposit is proposed to have formed during the Late Triassic period (ca. 217–207 Ma). This temporal constraint corresponds to the post-collisional extensional setting in the EKOB, induced by lithospheric delamination. This hypothesis is supported by various lines of evidence, including abundant extension-related alkaline mafic dyke swarms, A-type granites, adakite-like granites, high Nb-Ta rhyolites, and bimodal volcanic rocks in the region (Xia et al., 2014; Hu et al., 2016; Yin et al., 2017; Zhou et al., 2020; Li et al., 2020b). Furthermore, there is a notable decreased in the crust thickness of EKOB during this period (Wu et al., 2019; Zhang et al., 2023).

Under the extensional tectonic setting, metals and sulfur were transported through magmatic-hydrothermal fluids. These substances were deposited within pre-existing fault zones due to fluid cooling and the decrease in pressure, coupled with decreases in fO2 and fS2. These fault zones exhibit a northwest trend in the Elashan Formation and an east–west trend in the Jinshuikou Group (Fig. 2a). As discussed above, the deposition of minerals in the Nageng deposit was primarily controlled by variations in the physicochemical conditions of the ore-forming fluids. The migration of these fluids from deeper to shallower parts resulted in a gradual cooling process. This cooling process led to the formation of quartz + pyrite veins and stockworks during stage 1, followed by the development of abundant and massive sulfides during stage 2. Subsequent cooling, accompanied by pressure reduction and a decrease in fO$_2$, played a crucial role in the precipitation of Ag sulfosalts, quartz, and calcite during stage 3. Consequently, the Nageng deposit exhibits a distinct metal zonation, with predominant Pb-Zn mineralization in deeper zones and prominent Ag mineralization in shallower zones (Fig. 12c; Chen et al., 2019; Chen et al., 2022b).

Therefore, the Nageng deposit can be classified as a typical magmatic-hydrothermal vein-type Ag-Pb-Zn deposit, which is characterized by the following features: (1) formation under an extensional
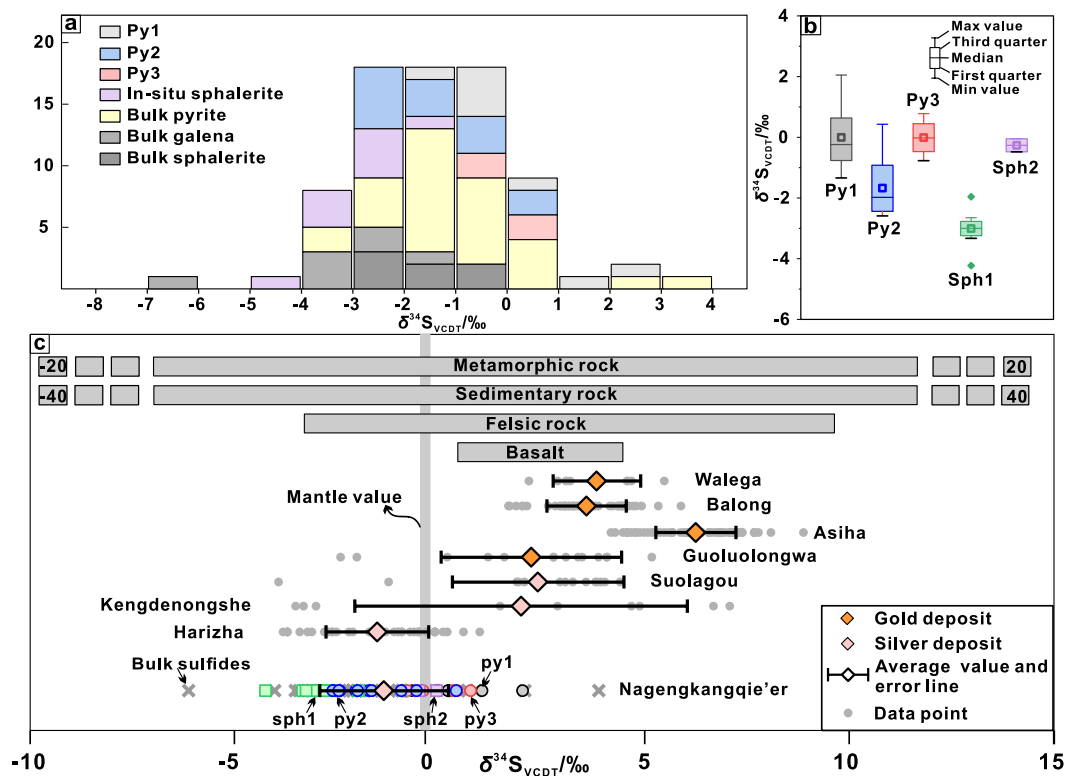
Fig. 10. Sulfur isotopic compositions of sulfide minerals from the Nagengkangqie'er deposit. (a) displays a histogram of both in situ and bulk sulfur isotope data. (b) compares the in situ and bulk sulfur isotopic compositions of sulfide minerals formed in different stages of mineralization process. (c) shows a comparison of sulfur isotopic compositions between the Nageng deposit and other gold and silver deposits in the EKOB. The bulk sulfur isotopic data are from Chen et al (2019), Xu et al (2020), Cheng. (2022). The δ^{34}S values of the other deposits are reported from (Jing et al., 2023).
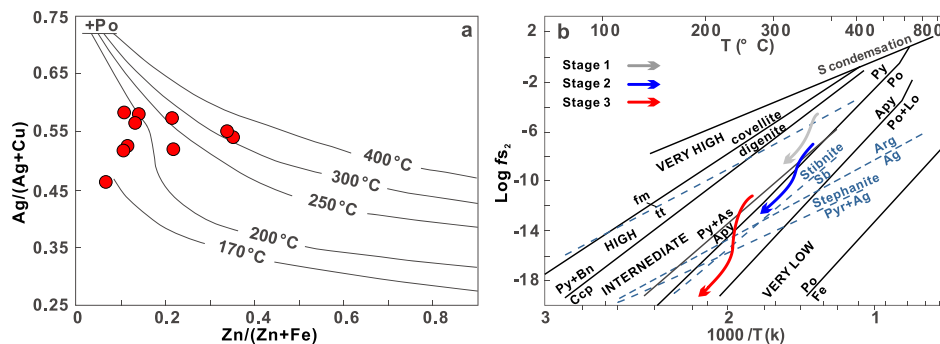

Fig. 11. (a) Molar Ag/ (Ag + Cu) vs. Zn/ (Zn + Fe) plot for primary freibergite in the Nageng deposit. The isotherms were calculated from Sack (2005). These isotherms terminate at low Zn/ (Zn + Fe) and high Ag/ (Ag + Cu) ratios because of saturation with respect to pyrrhotite (Po) (Balabin and Sack, 2000). (b) LogFS2 vs. temperature diagram showing the relative sulfidation state and the evolutionary path of hydrothermal fluids in the Nageng deposit. Temperatures were estimated from fluid inclusions (Chen et al., 2019) and sulfide studies, and logfS2 values from equilibrium mineral assemblages. Sulfidation state determinations and sulfidation reactions are from Li et al. (2019).

tectonic setting, (2) derived from magmatic-hydrothermal fluids and sources, (3) occur within faults, and characterized by vein or fracture-filling mineralization, (4) moderate to low mineralization temperatures ranging from 170 to 330 °C, with a salinity of 4 to 7 wt% NaCl equivalent (Li and Li, 2017; Chen et al., 2019), and (5) mineral assemblages composed of diverse sulfides, Ag-bearing sulfosalts, as well as quartz and calcite as the main gangue minerals. These features align the Nageng Ag deposit with other well-known vein-type Ag-Pb-Zn deposits found worldwide, including the Butte Main Stage veins in Montana (USA) (Lund et al., 2018), Keno Hill district in Yukon (Canada) (Lynch et al., 1990; Sack and Lichtner, 2009), and the Bianjiadayuan, Shuangjianzishan and Xiasai deposits in China (Li et al., 2019; Li et al., 2020a; Zhai et al., 2018; Zhai et al., 2020).

7. Conclusions

(1) The Nageng deposit can be categorized as a typical magmatic-hydrothermal vein-type Ag-Pb-Zn deposit. Noteworthy quantities of silver are found within minerals such as pyrargyrite, freibergite, and stephanite.

(2) Based on post-ore calcite U-Pb dating, the formation of the Nageng Ag deposit is estimated to have occurred between approximately 217–207 Ma within a post-collisional setting of the East Kunlun Orogenic Belt (EKOB).

(3) The in-situ sulfur isotopic compositions of pyrite and sphalerite at Nageng silver deposit indicate that ore-forming materials were derived from felsic magmas.
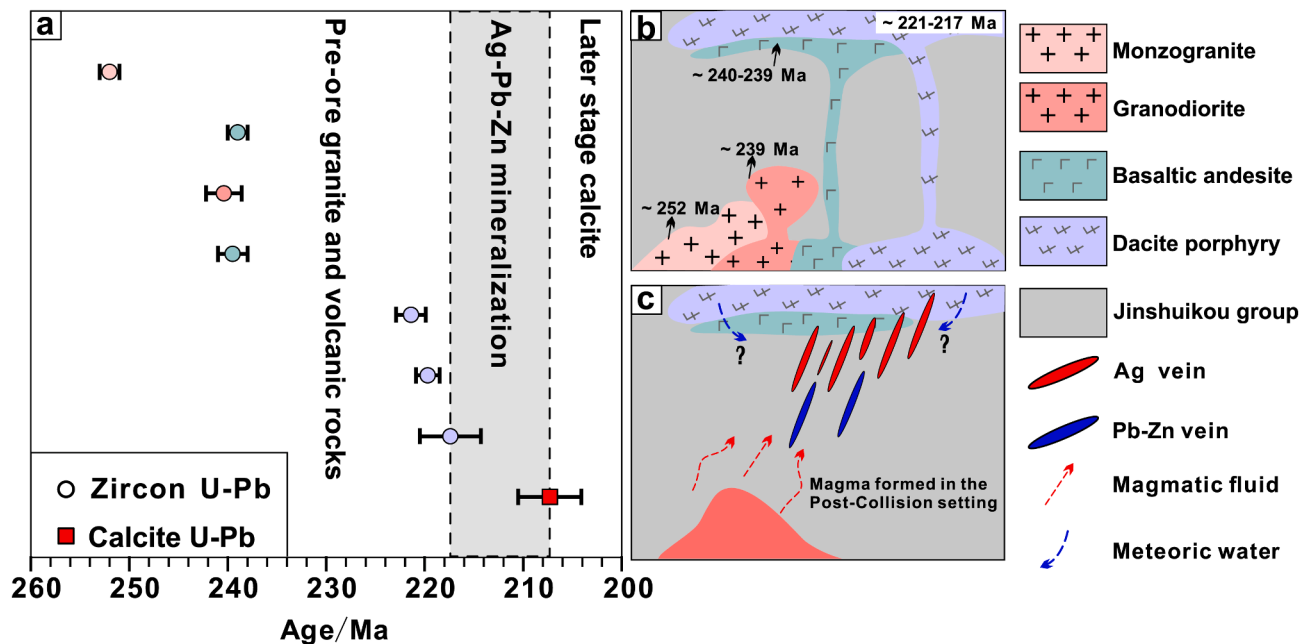
Fig. 12. (a) A chronology of magmatic and mineralization events in the Nagengkanqie'er deposit. Data are listed in Table 1. The uncertainty for all data is 2σ; (b) and (c) cartoons illustrating the sequence of magmatic, volcanic, and mineralizing events from ~ 252 to 207 Ma in the Nagengkanqie'er ore district.

(4) In-situ trace elements and sulfur isotopic compositions of pyrite indicate the formation of Ag–Pb–Zn veins were triggered by a decrease in temperature, fS_2, and fO_2.

Declaration of Competing Interest

The authors declare that they have no known competing financial interests or personal relationships that could have appeared to influence the work reported in this paper.

Data availability

Data will be made available on request.

Appendix A. Supplementary data

Supplementary data to this article can be found online at https://doi.org/10.1016/j.oregeorev.2023.105696.

References

Balabin, A.I., Sack, R.O., 2000. Thermodynamics of (Zn, Fe)S sphalerite; a CVM approach with large basis clusters. Mineral. Mag. 64 (426), 923–943. https://doi.org/10.1180/002646100549751.

Baumgartner, R., Fontbote, L., Vennemann, T., 2008. Mineral zoning and geochemistry of epithermal polymetallic Zn-Pb-Ag-Cu-Bi mineralization at Cerro de Pasco. Peru. Econ Geol. 103 (3), 493–537. https://doi.org/10.2113/gsecongeo.103.3.493.

Bendall, C., Lahaye, Y., Fiebig, J., Weyer, S., Brey, G.P., 2006. In situ sulfur isotope analysis by laser ablation MC-ICPMS. Appl. Geochem. 21 (5), 782–787. https://doi.org/10.1016/j.apgeochem.2006.02.012.

Benites, D., Torró, L., Vallance, J., Laurent, O., Quispe, P., Rosas, S., Uzieda, M.F., Holm-Denoma, C.S., Pianowski, L.S., Camprubí, A., Colás, V., Fernández-Baca, Á., Giraldo, L., Chelle-Michou, C., Sáez, J., Kouzmanov, K., Fontboté, L., 2022. Geology, mineralogy, and cassiterite geochronology of the Ayawilca Zn-Pb-Ag-In-Sn-Cu deposit, Pasco. Peru. Miner Deposita. 57 (3), 481–507. https://doi.org/10.1007/s00126-021-01066-z.

Börner, F., Keith, M., Smith, D.J., Barry, T.L., Neumann, T., Klemd, R., 2021. Fingerprinting fluid evolution by trace elements in epithermal pyrite, Vatukoula Au-Te deposit. Fiji. Ore Geol Rev. 137, 104314 https://doi.org/10.1016/j.oregeorev.2021.104314.

Börner, F., Keith, M., Bücker, J.L., Voudouris, P., Klemd, R., Haase, K., Kutzschbach, M., Schiperski, F., 2022. In-situ trace element and S isotope systematics in pyrite from three porphyry-epithermal prospects, Limnos Island. Greece. Front. Earth Sci. 10 https://doi.org/10.3389/feart.2022.916107.

Borojević Šoštarić, S., Palinkaš, L.A., Topa, D., Spangenberg, J.E., Prochaska, W., 2011. Silver–base metal epithermal vein and listwaenite types of deposit Crnac, Rogozna Mts., Kosovo. Part I: Ore mineral geochemistry and sulfur isotope study. Ore Geol. Rev. 40 (1), 65–80. https://doi.org/10.1016/j.oregeorev.2011.05.002.

Borojević Šoštarić, S., Palinkaš, L.A., Neubauer, F., Hurai, V., Cvetković, V., Roller-Lutz, Z., Mandić, M., Genser, J., 2013. Silver-base metal epithermal vein and listwanite hosted deposit Crnac, Rogozna Mts., Kosovo, part II: A link between magmatic rocks and epithermal mineralization. Ore Geol. Rev. 50, 98–117. https://doi.org/10.1016/j.oregeorev.2012.10.005.

Chen, X.H., Gehrels, G., Yin, A., Li, L., Jiang, R.B., 2012. Paleozoic and mesozoic basement magmatisms of Eastern Qaidam Basin, Northern Qinghai-Tibet Plateau: LA-ICP-MS zircon U-Pb geochronology and its geological significance. Acta Geol. Sinica (English Edition). 86 (2), 350–369. https://doi.org/10.1111/j.1755-6724.2012.00665.x.

Chen, X.D., Li, Y.G., Li, M.T., Zhou, H.B., Sun, C.B., Zhao, Y.C., Lai, C.K., 2019. Ore geology, fluid inclusions, and C-H–O–S–Pb isotopes of Nagengkangqieergou Ag-polymetallic deposit, East Kunlun Orogen. NW China. Geol J. 55 (4), 2572–2590. https://doi.org/10.1002/gj.3526.

Chen, X.D., Li, B., Sun, C.B., Zhou, H.B., 2021. Protracted storage for calc-alkaline andesitic magma in magma chambers: Perspective from the Nageng andesite, East Kunlun Orogen. NW China. Minerals-Basel. 11 (2), 198. https://doi.org/10.3390/min11020198.

Chen, X.D., Li, B., Yu, M., Zhang, W.D., Zhu, L., 2022a. Generation of crystal-rich rhyodacites by fluid-induced crystal-mush rejuvenation: Perspective from the Late Triassic Nageng (sub-)volcanic complex of the East Kunlun Orogen. NW China. Chem Geol. 599, 120833 https://doi.org/10.1016/j.chemgeo.2022.120833.

Chen, X.D., Li, B., Tang, L., Zhang, W.D., Zhu, L., 2022b. Silver enrichment and trace element deportment in hydrothermal replacement reactions: Perspective from the Nageng Ag-polymetallic deposit, East Kunlun Orogen, NW China. Ore Geol Rev. 142, 104691 https://doi.org/10.1016/j.oregeorev.2021.104691.

Chen, J.J., Wei, J.H., Fu, L.B., Li, H., Zhou, H.Z., Zhao, X., Zhan, X.F., Tan, J., 2017. Multiple sources of the Early Mesozoic Gouli batholith, Eastern Kunlun Orogenic Belt, Northern Tibetan Plateau: Linking continental crustal growth with oceanic subduction. Lithos 292, 161–178. https://doi.org/10.1016/j.lithos.2017.09.006.

Chen, J.J., Fu, L.B., Selby, D., Wei, J.H., Zhao, X., Zhou, H.Z., 2020. Multiple episodes of gold mineralization in the East Kunlun Orogen, western Central Orogenic Belt,

China: Constraints from Re-Os sulfide geochronology. Ore Geol. Rev. 123, 103587 https://doi.org/10.1016/j.oregeorev.2020.103587.

Cheng, T., Zhao, J.X., Feng, Y.X., Pan, W.Q., Liu, D.Y., 2019. In-situ LA-MC-ICPMS U-Pb dating method for low-uranium carbonate minerals. Chin. Sci. Bull. 65 (2–3), 150–154. https://doi.org/10.1360/TB-2019-0355.

Cheng, J., 2022. LA-ICP-MS In-situ trace elements and S-Pb isotope characteristics of pyrite from Nageng silver deposit, East Kunlun. Miner Petrol, 42(01): 23-32, in Chinese with English abstract.

Clark, C., Grguric, B., Mumm, A.S., 2004. Genetic implications of pyrite chemistry from the Paleoproterozoic Olary Domain and overlying Neoproterozoic Adelaidean sequences, northeastern South Australia. Ore Geol. Rev. 25 (3–4), 237–257. https://doi.org/10.1016/j.oregeorev.2004.04.003.

Cong, D.G., Yuan, F., Pan, T., Wang, B.Z., Huang, G.B., Yu, F.C., Yuan, E.J., Li, S.W., Zhang, T.J., E, z.y.,, 2023. Genesis of the Heihaibei gold deposit in the East Kunlun Orogenic Belt, China: Evidence from in situ trace elements of gold-bearing sulfides and stable isotopes. Ore Geol. Rev. 157, 105431 https://doi.org/10.1016/j.oregeorev.2023.105431.

Corral, I., 2020. New 40Ar/39Ar dating of Alunite from the Cerro Quema Au-Cu Deposit, Azuero Peninsula, Panama. Econ. Geol. 116 (1), 211–226. https://doi.org/10.5382/econgeo.4776.

Dai, J.G., Wang, C.S., Hourigan, J., Santosh, M., 2013. Multi-stage tectono-magmatic events of the Eastern Kunlun Range, northern Tibet: Insights from U-Pb geochronology and (U–Th)/He thermochronology. Tectonophysics 599, 97–106. https://doi.org/10.1016/j.tecto.2013.04.005.

Deditius, A.P., Utsunomiya, S., Reich, M., Kesler, S.E., Ewing, R.C., Hough, R., Walshe, J., 2011. Trace metal nanoparticles in pyrite. Ore Geol. Rev. 42 (1), 32–46. https://doi.org/10.1016/j.oregeorev.2011.03.003.

Deng, J., Wang, Q.F., Sun, X., Yang, L., Groves, D.I., Shu, Q.H., Gao, L., Yang, L.Q., Qiu, K.F., Wang, C.M., Dong, C.Y., 2022. Tibetan ore deposits: A conjunction of accretionary orogeny and continental collision. Earth Sci. Rev. 104245 https://doi.org/10.1016/j.earscirev.2022.104245.

Dong, G.C., Luo, M.F., Mo, X.X., Zhao, Z.D., Dong, L.Q., Yu, X.H., Wang, X., Li, X.W., Huang, X.F., Liu, Y.B., 2018. Petrogenesis and tectonic implications of early Paleozoic granitoids in East Kunlun Belt: Evidences from geochronology, geochemistry and isotopes. Geosci. Front. 9 (5), 1383–1397. https://doi.org/10.1016/j.gsf.2018.03.003.

Dong, Y.P., Sun, S.S., Santosh, M., Hui, B., Sun, J.P., Zhang, F.F., Cheng, B., Yang, Z., Shi, X.H., He, D.F., Cheng, C., Liu, X.M., Zhou, X.H., Wang, W., Qi, N., 2022. Cross Orogenic Belts in Central China: Implications for the tectonic and paleogeographic evolution of the East Asian continental collage. Gondw. Res. 109, 18–88. https://doi.org/10.1016/j.gr.2022.04.012.

Elatikpo, S.M., Li, H., Liu, B., Zhang, W.D., 2022. Metallogenesis of the Bakoshi-Kundila gold deposit in northern West Nigerian Subshield: Insights from pyrite chemical and sulfur isotopic compositions and zircon U-Pb geochronology. Precambr. Res. 383, 106890 https://doi.org/10.1016/j.precamres.2022.106890.

Fan, H.R., Hu, F.F., Yang, K.F., Pirajno, F., Liu, X., Wang, K.Y., 2014. Integrated U-Pb and Sm–Nd geochronology for a REE-rich carbonatite dyke at the giant Bayan Obo REE deposit. Northern China. Ore Geol Rev. 63, 510–519. https://doi.org/10.1016/j.oregeorev.2014.03.005.

Fan, X.Z., Sun, F.Y., Xu, C.H., Xin, W., Wang, Y.C., Zhang, Y., 2021. Genesis of Harizha Ag–Pb–Zn deposit in the eastern Kunlun Orogen, NW China: Evidence of fluid inclusions and C-H–O–S–Pb isotopes. Resour. Geol. 71 (3), 177–201. https://doi.org/10.1111/rge.12256.

Feng, C.Y., Li, D.S., Wu, Z.S., Li, J.H., Zhang, Z.Y., Zhang, A.K., Shu, X.F., Su, S.S., 2010. Major types, time-space distribution and metallogenies of polymetallic deposits in the Qimantage metallogenic belt, Eastern Kunlun area. Northwestern. Geology 43 (04), 10–17 in Chinese with English abstract.

Gammons, C.H., Barnes, H.L., 1989. The solubility of Ag2S in near-neutral aqueous sulfide solutions at 25 to 300°C. Geochim Cosmochim Ac. 53 (2), 279–290. https://doi.org/10.1016/0016-7037(89)90380-3.

Grandia, F., Asmerom, Y., Getty, S., Cardellach, E., Canals, A., Pueyo, J.J., Cardellach, E., Bitzer, K., Taberner, C., 2000. U-Pb dating of MVT ore-stage calcite; implications for fluid flow in a Mesozoic extensional basin from Iberian Peninsula. J. Geochem. Explor. 69–70, 377–380. https://doi.org/10.1016/S0375-6742(00)00030-3.

Grant, H.L.J., Hannington, M.D., Petersen, S., Frische, M., Fuchs, S.H., 2018. Constraints on the behavior of trace elements in the actively-forming TAG deposit, Mid-Atlantic Ridge, based on LA-ICP-MS analyses of pyrite. Chem. Geol. 498, 45–71. https://doi.org/10.1016/j.chemgeo.2018.08.019.

Gregory, D.D., Large, R.R., Halpin, J.A., Baturina, E.L., Lyons, T.W., Wu, S., Danyushevsky, L., Sack, P.J., Chappaz, A., Maslennikov, V.V., Bull, S.W., 2015. Trace Element Content of Sedimentary Pyrite in Black Shales*. Econ. Geol. 110 (6), 1389–1410. https://doi.org/10.2113/econgeo.110.6.1389.

Grema, H.M., Magnall, J.M., Whitehouse, M.J., Gleeson, S.A., Schulz, H., 2022. The Formation of Highly Positive δ34S Values in Late Devonian Mudstones: Microscale Analysis of Pyrite (δ34S) and Barite (δ34S, δ18O) in the Canol Formation (Selwyn Basin, Canada). Front. Earth Sci. 9 https://doi.org/10.3389/feart.2021.784824.

Guo, X.Z., 2020. The Intermediate-acid Magmatism and Polymetallic Mineralization in East Kunlun, Paleo-Tethys. In: Chinese with English Abstract. China University of Geosciences (Wuhan), p. 246 pp,. Ph. D Thesis,.

Guo, X.Z., Xie, W.H., Zhou, H.B., Tian, C.S., Li, J.C., Kong, H.L., Yang, T., Yao, X.G., Jia, Q.Z., 2019. Zircon U-Pb Chronology and Geochemistry of the Rhyolite Porphyry in the Nagengkangqie'er Silver Polymetallic Deposit, East Kunlun and Their Geological Significance. Earth Sci. 44 (07), 2505–2518 in Chinese with English abstract.

Han, R., Qin, K.Z., Groves, D.I., Hui, K.X., Li, Z.Z., Zou, X.Y., Li, G.M., Su, S.Q., 2022. Ore-formation at the Halasheng Ag-Pb-Zn deposit, northeast Inner Mongolia as revealed

by trace-element and sulfur isotope compositions of ore-related sulfides. Ore Geol. Rev. 144, 104853 https://doi.org/10.1016/j.oregeorev.2022.104853.

Haynes, S.J., 1993. Vein-type ore deposits: Introduction. Ore Geol. Rev. 8 (3), 205–211. https://doi.org/10.1016/0169-1368(93)90016-R.

Hu, Y., Niu, Y.L., Li, J.Y., Ye, L., Kong, J.J., Chen, S., Zhang, Y., Zhang, G.R., 2016. Petrogenesis and tectonic significance of the late Triassic mafic dikes and felsic volcanic rocks in the East Kunlun Orogenic Belt, Northern Tibet Plateau. Lithos 245, 205–222. https://doi.org/10.1016/j.lithos.2015.05.004.

Huang, X.K., 2021. Gold Mineralization and Comprehensive Information Prospecting Prediction in Balong-Gouli Area, East Kunlun Orogen. In: Chinese with English Abstract. China University of Geosciences, p. 223 pp,. Ph. D Thesis,.

Huang, X.K., Wei, J.H., Li, H., Chen, M.T., Wang, Y.L., Li, G.M., Yan, M.Q., Zhang, X.M., 2021. Zircon U-Pb geochronology, elemental and Sr-Nd-Hf isotopic constraints on petrogenesis of the Late Triassic quartz diorite in Balong region, East Kunlun Orogen. Earth Sci. 46 (06), 2037–2056 in Chinese with English abstract.

Huston, D.L., Sie, S.H., Suter, G.F., Cooke, D.R., Both, R.A., 1995. Trace elements in sulfide minerals from eastern Australian volcanic-hosted massive sulfide deposits; Part I, Proton microprobe analyses of pyrite, chalcopyrite, and sphalerite, and Part II, Selenium levels in pyrite; comparison with delta 34 S values and implications for the source of sulfur in volcanogenic hydrothermal systems. Econ. Geol. 90 (5), 1167–1196. https://doi.org/10.2113/gsecongeo.90.5.1167.

Ishida, M., Romero, R., Leisen, M., Yasukawa, K., Nakamura, K., Barra, F., Reich, M., Kato, Y., 2022. Auriferous pyrite formed by episodic fluid inputs in the Akeshi and Kasuga high-sulfidation deposits, Southern Kyushu, Japan. Miner Deposita. 57 (1), 129–145. https://doi.org/10.1007/s00126-021-01053-4.

Jansson, N.F., Zetterqvist, A., Allen, R.L., Billström, K., Malmström, L., 2017. Genesis of the Zinkgruvan stratiform Zn-Pb-Ag deposit and associated dolomite-hosted Cu ore, Bergslagen. Sweden. Ore Geol Rev. 82, 285–308. https://doi.org/10.1016/j.oregeorev.2016.12.004.

Jean-Philippe, P., Georges, B., Suzanne, P., Thomas, U., 2012. Geochemistry and metallogeny of Ag-Pb-Zn veins in the Purcell Basin, British Columbia. Econ. Geol. 107 (6), 1303–1320. https://doi.org/10.2113/econgeo.107.6.1303.

Jiang, B., Zhang, D.Q., Wang, D.H., Wang, C.H., Chen, Y.C., Bai, G., 2015. A Preliminary Review of Metallogenic Regularity of Silver Deposits in China. Acta Geol. Sin. – Engl. Ed. 89 (3), 1002–1020. https://doi.org/10.1111/1755-6724.12493.

Jin, X.Y., Zhao, J.X., Feng, Y.X., Hofstra, A.H., Deng, X.D., Zhao, X.F., Li, J.W., 2021. Calcite U-Pb dating unravels the age and hydrothermal history of the giant Shuiyindong carlin-type gold deposit in the golden triangle, South China. Econ. Geol. 116 (6), 1253–1265. https://doi.org/10.5382/econgeo.4870.

Jing, G.Z., Wang, X.Y., Zhang, Z.Q., He, J.J., Zhang, L.B., Wang, F.L., Liu, Y., Shi, W.J., Tan, J., 2023. Middle-late Triassic regional-scale magmatic-hydrothermal metallogenic system in the eastern segment of the East Kunlun. Bull. Geol. Sci. Technol. 42 (01), 89–111 in Chinese with English abstract.

Kamaunji, V.D., Wang, L.X., Ma, C.Q., Liu, J., Zhu, Y.X., 2020. Petrogenesis and tectonic implication of the Permian-Triassic syenogranites from the eastern segment of the East Kunlun Orogen, China. Lithos 105932. https://doi.org/10.1016/j.lithos.2020.105932.

Keith, M., Haase, K.M., Schwarz-Schampera, U., Klemd, R., Petersen, S., Bach, W., 2014. Effects of temperature, sulfur, and oxygen fugacity on the composition of sphalerite from submarine hydrothermal vents. Geology (Boulder). 42 (8), 699–702. https://doi.org/10.1130/G35655.1.

Keith, M., Häckel, F., Haase, K.M., Schwarz-Schampera, U., Klemd, R., 2016. Trace element systematics of pyrite from submarine hydrothermal vents. Ore Geol. Rev. 72, 728–745. https://doi.org/10.1016/j.oregeorev.2015.07.012.

Keith, M., Smith, D.J., Doyle, K., Holwell, D.A., Jenkin, G.R.T., Barry, T.L., Becker, J., Rampe, J., 2020. Pyrite chemistry: A new window into Au-Te ore-forming processes in alkaline epithermal districts, Cripple Creek, Colorado. Geochim. Cosmochim. Ac. 274, 172–191. https://doi.org/10.1016/j.gca.2020.01.056.

Kelley, K.D., Leach, D.L., Johnson, C.A., Clark, J.L., Fayek, M., Slack, J.F., Anderson, V. M., Ayuso, R.A., Ridley, W.I., 2004. Textural, compositional, and sulfur isotope variations of sulfide minerals in the red dog Zn-Pb-Ag deposits, Brooks Range, Alaska: Implications for Ore Formation. Econ. Geol. 99 (7), 1509–1532. https://doi.org/10.2113/gsecongeo.99.7.1509.

Kendrick, M.A., Plümper, O., Zhao, J., Defliese, W.F., Müller, I.A., Ziegler, M., 2022. Exhumation and carbonation of the Atlantis Bank core complex constrained by in situ U-Pb dating and Δ47 thermometry of calcite veins, SW Indian Ridge. Earth Planet Sc Lett. 584, 117474 https://doi.org/10.1016/j.epsl.2022.117474.

Kouhestani, H., Ghaderi, M., Large, R.R., Zaw, K., 2017. Texture and chemistry of pyrite at Chah Zard epithermal gold–silver deposit. Iran. Ore Geol Rev. 84, 80–101. https://doi.org/10.1016/j.oregeorev.2017.01.002.

Kouhestani, H., Mokhtari, M.A.A., Chang, Z., Qin, K., Aghajani Marsa, S., 2022. Fluid inclusion, zircon U-Pb geochronology, and O-S isotopic constraints on the origin and evolution of ore-forming fluids of the tashvir and varmazyar epithermal base metal deposits, NW Iran. Front. Earth Sci. 10 https://doi.org/10.3389/feart.2022.990761.

Kreissl, S., Gerdes, A., Walter, B.F., Neumann, U., Wenzel, T., Markl, G., 2018. Reconstruction of a >200 Ma multi-stage "five element" Bi-Co-Ni-Fe-As-S system in the Penninic Alps, Switzerland. Ore Geol Rev. 95, 746–788. https://doi.org/10.1016/j.oregeorev.2018.02.008.

Kurumada, Y., Aoki, S., Aoki, K., Kato, D., Saneyoshi, M., Tsogtbaatar, K., Windley, B.F., Ishigaki, S., 2020. Calcite U-Pb age of the Cretaceous vertebrate-bearing Bayn Shire Formation in the Eastern Gobi Desert of Mongolia: Usefulness of caliche for age determination. Terra Nova 32 (4), 246–252. https://doi.org/10.1111/ter.12456.

Lehner, S.W., Savage, K.S., Ayers, J.C., 2006. Vapor growth and characterization of pyrite (FeS2) doped with Co, Ni, and As: Variations in semiconducting properties. J. Cryst. Growth 286 (2), 306–317. https://doi.org/10.1016/j.jcrysgro.2005.09.062.

Li, X.H., Fan, H.R., Liang, G.Z., Zhu, R.X., Yang, K.F., Steele-MacInnis, M., Hu, H.L., 2021a. Texture, trace elements, sulfur and He-Ar isotopes in pyrite: Implication for ore-forming processes and fluid source of the Guoluolongwa gold deposit, East Kunlun metallogenic belt. Ore Geol. Rev. 136, 104260 https://doi.org/10.1016/j. oregeorev.2021.104260.

Li, M.T., Li, Z.Q., 2017. Constrains of S-Pb-C-O Isotope Compositions on the Origin of Nagengkangqieer Silver Deposit, the Eastern Kunlun Mountains, China. Acta Mineral. Sin. 37 (6) in Chinese with English abstract.

Li, J.L., Lu, H.F., Chen, J., Tang, J., Li, J.Q., Fu, Y.W., 2017. Ore-control factors of Silver polymetallic mineralization in the east section of East Kunlun and prospecting potential of the area. Contrib. Geol. Miner. Resour. Res. 32 (2), 172–179 in Chinese with English abstract.

Li, Z.C., Pei, X.Z., Bons, P.D., Li, R.B., Pei, L., Chen, G.C., Chen, Y.X., Liu, C.J., Wang, M., Zhao, S.W., Li, X.B., Gao, F., 2021b. Petrogenesis and tectonic setting of the early-middle Triassic subduction-related granite in the eastern segment of East Kunlun: evidences from petrology, geochemistry, and zircon U-Pb-Hf isotopes. Int. Geol. Rev. 1–24 https://doi.org/10.1080/00206814.2021.1875268.

Li, H.R., Qian, Y., Sun, F.Y., Sun, J.L., Wang, G., 2020a. Zircon U-Pb dating and sulfide Re–Os isotopes of the Xiarihamu Cu–Ni sulfide deposit in Qinghai Province, Northwestern China. Can J Earth Sci. 57 (8), 885–902. https://doi.org/10.1139/cjes-2019-0107.

Li, Y.J., Wei, J.H., Ulrich, T., Chen, M.T., Li, H.M., Niu, M.W., Liu, B., 2019. Mineral chemistry of the Xiasai Ag–Pb–Zn deposit in the central Yidun Terrane, SW China: Insight into Ni–Ag–Bi mineralization and formation conditions. Ore Geol. Rev. 114, 103136 https://doi.org/10.1016/j.oregeorev.2019.103136.

Li, Y.J., Wei, J.H., Tan, J., Fu, L.B., Li, H., Ke, K.J., 2020b. Albian-Cenomanian A-type granite-related Ag–Pb–Zn veins in the central Yidun Terrane, SW China: constraints from the Xiasai deposit. Miner. Deposita 55 (6), 1047–1070. https://doi.org/10.1007/s00126-019-00920-5.

Li, Y.J., Wei, J.H., Santosh, M., Li, H., Liu, H.W., Niu, M.W., Liu, B., 2020c. Anisian granodiorites and mafic microgranular enclaves in the eastern Paleo-Tethys. Geol. J. 55 (9), 6487–6507. https://doi.org/10.1002/gj.3814.

Li, Y.J., Zhang, R.Q., Ji, H., Wang, C., Tan, J., Wei, J.H., 2022. Chemistry and U-Pb geochronology of cassiterite in the Xiasai deposit, central Yidun Terrane (SW China): Link between Sn and Ag–Pb–Zn mineralisation. Ore Geol. Rev. 149, 105106 https://doi.org/10.1016/j.oregeorev.2022.105106.

Li, Y.J., Wei, J.H., Chen, M.T., Chen, Z.H., Lahaye, Y., Zhang, H.J., Ulrich, T., 2023b. Molybdenum mineralization genetically linked with magmatism at the Shipingchuan deposit, SE China. GSA Bull. https://doi.org/10.1130/B36600.1.

Li, H., Zhu, D.P., Algeo, T.J., Li, M., Jiang, W.C., Chen, S.F., Elatikpo, S.M., 2023a. Pyrite trace element and S-Pb isotopic evidence for contrasting sources of metals and ligands during superimposed hydrothermal events in the Dongping gold deposit, North China. Miner Deposita 58 (2), 337–358. https://doi.org/10.1007/s00126-022-01128-w.

Liang, G.Z., Yang, K.F., Sun, W.Q., Fan, H.R., Li, X.H., Lan, T.G., Hu, H.L., Chen, Y.W., 2021. Multistage ore-forming processes and metal source recorded in texture and composition of pyrite from the Late Triassic Asiha gold deposit, Eastern Kunlun Orogenic Belt, western China. J. Asian Earth Sci. 220, 104920 https://doi.org/10.1016/j.jseaes.2021.104920.

Liu, Y.S., Hu, Z.C., Gao, S., Günther, D., Xu, J., Gao, C.G., Chen, H.H., 2008. In situ analysis of major and trace elements of anhydrous minerals by LA-ICP-MS without applying an internal standard. Chem. Geol. 257 (1–2), 34–43. https://doi.org/10.1016/j.chemgeo.2008.08.004.

Lu, H.F., Yang, Y.Q., He, J., Li, J.Q., 2017. Zircon U-Pb age dating for granodiorite porphyry and molybdenite Re-Os isotope dating of Halongxiuma molybdenum (tungsten) deposit in the East Kunlun area and its geological significance. Journal of. Mineral. Petrol. 37 (02), 33–39 in Chinese with English abstract.

Lund, K., McAleer, R.J., Aleinikoff, J.N., Cosca, M.A., Kunk, M.J., 2018. Two-event lode-ore deposition at Butte, USA: 40Ar/39Ar and U-Pb documentation of Ag-Au-polymetallic lodes overprinted by younger stockwork Cu-Mo ores and penecontemporaneous Cu lodes. Ore Geol. Rev. 102, 666–700. https://doi.org/10.1016/j.oregeorev.2018.05.018.

Luo, K., Zhou, J.X., Feng, Y.X., Uysal, I.T., Nguyen, A., Zhao, J.X., Zhang, J., 2020. In situ U-Pb dating of calcite from the South China Antimony Metallogenic Belt. iScience. 23 (10), 101575 https://doi.org/10.1016/j.isci.2020.101575.

Lynch, J.V.G., Longstaffe, F.J., Nesbitt, B.E., 1990. Stable isotopic and fluid inclusion indications of large-scale hydrothermal paleoflow, boiling, and fluid mixing in the Keno Hill Ag-Pb-Zn district, Yukon Territory. Canada. Geochim Cosmochim Ac. 54 (4), 1045–1059. https://doi.org/10.1016/0016-7037(90)90438-Q.

Mango, H., Arehart, G., Oreskes, N., Zantop, H., 2014. Origin of epithermal Ag–Au–Cu–Pb–Zn mineralization in Guanajuato. Mexico. Miner Deposita. 49 (1), 119–143. https://doi.org/10.1007/s00126-013-0478-z.

Mao, J.W., Cheng, Y.B., Chen, M.H., Franco, P., 2013a. Major types and time–space distribution of Mesozoic ore deposits in South China and their geodynamic settings. Miner. Deposita 48 (3), 267–294. https://doi.org/10.1007/s00126-012-0446-z.

Mao, J.W., Chen, Y.B., Chen, M.H., Franco, P., 2013b. Major types and time–space distribution of Mesozoic ore deposits in South China and their geodynamic settings. Miner. Deposita 48 (3), 267–294. https://doi.org/10.1007/s00126-012-0446-z.

Martin, A.J., Jamieson, J.W., de Ronde, C.E.J., Layne, G.D., Piercey, G., Brandl, P.A., 2023. Constraining temporal variations in metal and sulfur sources using high-resolution mineral-scale analysis of pyrite: evidence from the Brothers volcano, Kermadec arc, New Zealand. Miner Deposita. https://doi.org/10.1007/s00126-023-01177-9.

Maslennikov, V.V., Maslennikova, S.P., Large, R.R., Danyushevsky, L.V., 2009. Study of trace element zonation in vent chimneys from the Silurian Yaman-Kasy volcanic-

hosted massive sulfide deposit (Southern Urals, Russia) using laser ablation-inductively coupled plasma mass spectrometry (LA-ICPMS). Econ. Geol. 104 (8), 1111–1141. https://doi.org/10.2113/gsecongeo.104.8.1111.

Mason, P.R.D., Košler, J., de Hoog, J.C.M., Sylvester, P.J., Meffan-Main, S., Naturvetenskapliga, F., Faculty, O.S., Göteborgs, U., Institutionen, F.G., Gothenburg, U., Department, O.E.S., 2006. In situ determination of sulfur isotopes in sulfur-rich materials by laser ablation multiple-collector inductively coupled plasma mass spectrometry (LA-MC-ICP-MS). J Anal. Atom Spectrom. 21 (2), 177–186. https://doi.org/10.1039/B510883G.

Mederer, J., Moritz, R., Zohrabyan, S., Vardanyan, A., Melkonyan, R., Ulianov, A., 2014. Base and precious metal mineralization in Middle Jurassic rocks of the Lesser Caucasus: A review of geology and metallogeny and new data from the Kapan, Alaverdi and Mehmana districts. Ore Geol. Rev. 58, 185–207. https://doi.org/10.1016/j.oregeorev.2013.10.007.

Morse, J.W., Luther, G.W., 1999. Chemical influences on trace metal-sulfide interactions in anoxic sediments. Geochim. Cosmochim. Ac. 63 (19), 3373–3378. https://doi.org/10.1016/S0016-7037(99)00258-6.

Nuriel, P., Wotzlaw, J., Ovtcharova, M., Vaks, A., Stremtan, C., Šala, M., Roberts, N.M. W., Kylander-Clark, A.R.C., 2021. The use of ASH-15 flowstone as a matrix-matched reference material for laser-ablation U − Pb geochronology of calcite. Geochronology. 3 (1), 35–47. https://doi.org/10.5194/gchron-3-35-2021.

Ohmoto, H., 1972. Systematics of Sulfur and Carbon Isotopes in Hydrothermal Ore Deposits. Econ. Geol. 67 (5), 551–578. https://doi.org/10.2113/gsecongeo.67.5.551.

Ohmoto, H., Rye, R.O., 1979. Carbon and sulfur isotopes, geochemistry of hydrothermal ore deposits. Wiley-Interscience New York 509–567.

Paiement, J., Beaudoin, G., Paradis, S., Ullrich, T., Box, S.E., Bookstrom, A.A., Anderson, R.G., 2012. Geochemistry and metallogeny of Ag-Pb-Zn veins in the Purcell Basin, British Columbia. Econ. Geol. 107 (6), 1303–1320. https://doi.org/10.2113/econgeo.107.6.1303.

Pan, G.T., Wang, L.Q., Li, R.S., Yuan, S.H., Ji, W.H., Yin, F.G., Zhang, W.P., Wang, B.D., 2012. Tectonic evolution of the Qinghai-Tibet Plateau. J. Asian Earth Sci. 53, 3–14. https://doi.org/10.1016/j.jseaes.2011.12.018.

Paton, C., Hellstrom, J., Paul, B., Woodhead, J., Hergt, J., 2011. Iolite: Freeware for the visualisation and processing of mass spectrometric data. J. Anal. At. Spectrom 26 (12), 2508. https://doi.org/10.1039/c1ja10172b.

Pavlovskaia, E.A., Khudoley, A.K., Ruh, J.B., Moskalenko, A.N., Guillong, M., Malyshev, S.V., 2022. Tectonic evolution of the northern Verkhoyansk Fold-and-Thrust Belt: insights from palaeostress analysis and U-Pb calcite dating. Geol. Mag. 1–25 https://doi.org/10.1017/S0016756822000528.

Pinet, N., Davis, W.J., Petts, D.C., Sack, P., Mercier-Langevin, P., Lavoie, D., Jackson, S. E., 2022. U-Pb vein calcite dating reveals the age of carlin-type gold deposits of central Yukon and a cpntemporaneity with a regional intrusion-related metallogenic event. Econ. Geol. https://doi.org/10.5382/econgeo.4898.

Pokrovski, G.S., Kokh, M.A., Proux, O., Hazemann, J., Bazarkina, E.F., Testemale, D., Escoda, C., Boiron, M., Blanchard, M., Aigouy, T., Gouy, S., de Parseval, P., Thibaut, M., 2019. The nature and partitioning of invisible gold in the pyrite-fluid system. Ore Geol. Rev. 109, 545–563. https://doi.org/10.1016/j.oregeorev.2019.04.024.

Reich, M., Deditius, A., Chryssoulis, S., Li, J., Ma, C., Parada, M.A., Barra, F., Mittermayr, F., 2013. Pyrite as a record of hydrothermal fluid evolution in a porphyry copper system: A SIMS/EMPA trace element study. Geochim Cosmochim Ac. 104, 42–62. https://doi.org/10.1016/j.gca.2012.11.006.

Renock, D., Becker, U., 2011. A first principles study of coupled substitution in galena. Ore Geol. Rev. 42 (1), 71–83. https://doi.org/10.1016/j.oregeorev.2011.04.001.

Roberts, N.M.W., Rasbury, E.T., Parrish, R.R., Smith, C.J., Horstwood, M.S.A., Condon, D.J., 2017. A calcite reference material for LA-ICP-MS U-Pb geochronology. Geochem. Geophys. Geosyst. 18 (7), 2807–2814. https://doi.org/10.1002/2016GC006784.

Román, N., Reich, M., Leisen, M., Morata, D., Barra, F., Deditius, A.P., 2019. Geochemical and micro-textural fingerprints of boiling in pyrite. Geochim Cosmochim Ac. 246, 60–85. https://doi.org/10.1016/j.gca.2018.11.034.

Rudnick, R.L., Gao, S., 2014. 4.1 - Composition of the continental crust. In: Holland, H. D., Turekian, K.K. (Eds.), Treatise on Geochemistry, second ed. Elsevier, Oxford, pp. 1–51.

Sack, R.O., 2005. Internally consistent database for sulfides and sulfosalts in the system Ag2S-Cu2S-ZnS-FeS-Sb2S3-As2S3: Update. Geochim. Cosmochim. Ac. 69 (5), 1157–1164. https://doi.org/10.1016/j.gca.2004.08.017.

Sack, R.O., Lichtner, P.C., 2009. Constraining compositions of hydrothermal fluids in equilibrium with polymetallic ore-forming sulfide assemblages. Econ. Geol. 104 (8), 1249–1264. https://doi.org/10.2113/gsecongeo.104.8.1249.

Savage, K.S., Stefan, D., Lehner, S.W., 2008. Impurities and heterogeneity in pyrite: Influences on electrical properties and oxidation products. Appl. Geochem. 23 (2), 103–120. https://doi.org/10.1016/j.apgeochem.2007.10.010.

Seward, T.M., 1976. The stability of chloride complexes of Silver in hydrothermal solutions up to 350°C. Geochim Cosmochim Ac. 40 (11), 1329–1341. https://doi.org/10.1016/0016-7037(76)90122-8.

Shan, L., Li, Y.J., Jiang, J.S., Bao, H., Huang, X.K., 2023. Magmatism and mineralization of the Taolin Pb–Zn–Cu deposit in the Mufushan area, central Jiangnan Orogen (South China): Insightful from zircon U-Pb and sphalerite Rb–Sr geochronology, and H–O–S–Pb isotope geochemistry. Ore Geol. Rev. 153, 105266 https://doi.org/10.1016/j.oregeorev.2022.105266.

Shannon, R., 1976. Revised effective ionic radii and systematic studies of interatomic distances in halides and chalcogenides. Acta Crystallogr. Sect. A: Found. Adv. 32 (5), 751–767. https://doi.org/10.1107/S0567739476001551.

Shen, A.J., Hu, A.P., Cheng, T., Liang, F., Pan, W.Q., Feng, Y.X., Zhao, J.X., 2019. Laser ablation in situ U-Pb dating and its application to diagenesis-porosity evolution of carbonate reservoirs. Petrol Explor Dev+. 46 (6), 1127–1140. https://doi.org/10.1016/S1876-3804(19)60268-5.

Sheng, X.Y., Tang, Y.Y., Bi, X.W., Hu, R.Z., Xu, L.L., Li, J., Tang, Y.W., 2022. In situ U-Pb dating of calcite indicates a Miocene Sb-Pb mineralization event in the Sanjiang base metal metallogenic belt, SW China. J. Geochem. Explor. 238, 107004 https://doi.org/10.1016/j.gexplo.2022.107004.

Simmons, S.F., White, N.C., John, D.A., Hedenquist, J.W., Thompson, J.F.H., Goldfarb, R. J., Richards, J.P., 2005. Geological characteristics of epithermal precious and base metal deposits, one hundredth anniversary volume. Soc. Econ. Geol. 455–522.

Stouraiti, C., Soukis, K., Voudouris, P., Mavrogonatos, C., Lozios, S., Lekkas, S., Beard, A., Strauss, H., Palles, D., Baziotis, I., Soulamidis, G., 2019. Silver-rich sulfide mineralization in the northwestern termination of the Western Cycladic Detachment System, at Agios Ioannis Kynigos, Hymittos Mt. (Attica, Greece): A mineralogical, geochemical and stable isotope study. Ore Geol. Rev. 111 https://doi.org/10.1016/j.oregeorev.2019.102992.

Su, J.B., Tan, H.B., Feng, Y.X., Qin, G.X., 2021. Syn-faulting calcite ages: constraint for the late mesozoic deformation of the ningzhen Mountain, Eastern China. J. Earth Sci. 32 (6), 1485–1495. https://doi.org/10.1007/s12583-020-1107-2.

Sykora, S., Cooke, D.R., Meffre, S., Stephanov, A.S., Gardner, K., Scott, R., Selley, D., Harris, A.C., 2018. Evolution of pyrite trace element compositions from porphyry-style and epithermal conditions at the lihir gold deposit: implications for ore genesis and mineral processing. Econ. Geol. 113 (1), 193–208. https://doi.org/10.5382/econgeo.2018.4548.

Vaughan, D.J., 2006. Sulfide mineralogy and geochemistry: introduction and overview. Rev. Mineral. Geochem. 61 (1), 1–5. https://doi.org/10.2138/rmg.2006.61.1.

Wang, F.X., Bagas, L., Jiang, S.H., Zhang, F.X., Liu, Y.F., Chong, X.X., 2019. Geochronology and ore genesis of the Shuangjianzishan Ag-polymetallic deposit, Inner Mongolia. China. Ore Geol Rev 107, 1020–1045. https://doi.org/10.1016/j.oregeorev.2019.03.026.

Wang, H., Feng, C.Y., Li, D.X., Li, C., Ding, T.Z., Liao, F.Z., 2016. Geology, geochronology and geochemistry of the Saishitang Cu deposit, East Kunlun Mountains, NW China: Constraints on ore genesis and tectonic setting. Ore Geol. Rev. 72, 43–59. https://doi.org/10.1016/j.oregeorev.2015.07.002.

Wang, W., Hu, Y., Muscente, A.D., Cui, H., Guan, C., Hao, J., Zhou, C., 2021b. Revisiting Ediacaran sulfur isotope chemostratigraphy with in situ nanoSIMS analysis of sedimentary pyrite. Geology 49 (6), 611–616. https://doi.org/10.1130/G48262.1.

Wang, K., Wang, L.X., Ma, G.G., Zhu, Y.X., Gao, L.Y., 2020. Petrogenesis and geological implications of the middle triassic garnet-bearing two-mica granite from Jialuhe Region, East Kunlun. Earth Sci. 45 (02), 400–418 in Chinese with English abstract.

Wang, K.X., Zhai, D.G., Liu, J.J., Wu, H., 2021a. LA-ICP-MS trace element analysis of pyrite from the Dafang gold deposit, South China: Implications for ore genesis. Ore Geol. Rev. 139, 104507 https://doi.org/10.1016/j.oregeorev.2021.104507.

Ward, J., Mavrogenes, J., Murray, A., Holden, P., 2017. Trace element and sulfur isotopic evidence for redox changes during formation of the Wallaby Gold Deposit, Western Australia. Ore Geol Rev 82, 31–48. https://doi.org/10.1016/j.oregeorev.2016.11.011.

Warr, L.N., 2021. IMA–CNMNC approved mineral symbols. MinMag. 85 (3), 291–320. https://doi.org/10.1180/mgm.2021.43.

Williams-Jones, A.E., Migdisov, A.A., Kelley, K.D., Golden, H.C., 2014. Experimental Constraints on the Transport and Deposition of Metals in Ore-Forming Hydrothermal Systems, Building Exploration Capability for the 21st Century. Soc. Econ. Geol.

Wilson, S.A., Ridley, W.I., Koenig, A.E., 2002. Development of sulfide calibration standards for the laser ablation inductively-coupled plasma mass spectrometry technique. J. Anal. Atom Spectrom. 17 (4), 406–409. https://doi.org/10.1039/B108787H.

Wu, J.J., Zeng, Q.D., Santosh, M., Fan, H.R., Wei, Z.H., Yang, K.F., Zhang, Z.M., Li, X.H., Liang, G.Z., 2021. Intrusion-related orogenic gold deposit in the East Kunlun belt, NW China: A multiproxy investigation. Ore Geol. Rev. 139, 104550 https://doi.org/10.1016/j.oregeorev.2021.104550.

Wu, C., Zuza, A.V., Chen, X.H., Ding, L., Levy, D.A., Liu, C.F., Liu, W.C., Jiang, T., Stockli, D.F., 2019. Tectonics of the Eastern Kunlun Range: cenozoic reactivation of a paleozoic-early mesozoic orogen. Tectonics 38 (5), 1609–1650. https://doi.org/10.1029/2018TC005370.

Xia, R., Wang, C.M., Deng, J., Carranza, E.J.M., Li, W.L., Qing, M., 2014. Crustal thickening prior to 220Ma in the East Kunlun Orogenic Belt: Insights from the Late Triassic granitoids in the Xiao-Nuomuhong pluton. J. Asian Earth Sci. 93, 193–210. https://doi.org/10.1016/j.jseaes.2014.07.013.

Xiao, Y., Feng, C.Y., Liu, J.N., Yu, M., Zhou, J.H., Li, D.X., Zhao, Y.M., 2013. LA-ICP-MS Zircon U-Pb dating and sulfur isotope characteristics of Kendekeke Fe-polymetallic deposit, Qinghai province. Mineral Deposits 32 (01), 177–186 in Chinese with English abstract.

Xu, J.W., Liu, X.H., Lai, J.Q., He, H.S., Song, X.F., Zhai, D.G., Li, B., Wang, Y.H., Shi, J., Zhou, X., 2022. In Situ U-Pb Geochronology of Calcite from the World's Largest Antimony Deposit at Xikuangshan, Southern China. Minerals-Basel. 12 (7), 899. https://doi.org/10.3390/min12070899.

Xu, C.W., Wei, J.H., Zhou, H.Z., Zhao, X., Zhang, S.T., Li, W.J., 2020. S-Pb isotope characteristics and prospecting model of the Nagengkangqieer silver deposit in the eastern segment of East Kunlun Mountain. Geol. Bull. China 39 (5), 712–727 in Chinese with English abstract.

Xu, Y.P., Xie, W.H., Yang, Y.F., He, Z.W., Wen, J., 2014. Geological Characteristics and Prospecting Perspective of Nagengkangqie'er Silver Deposit in Eastern Kunlun Mountain of Qinghai. Xinjiang. Geology 1, 113–117 in Chinese with English abstract.

Yan, X., Chen, B., Duan, X., Wang, Z., 2021. Geochronology and Ore Genesis of the Niujuan-Yingfang Pb-Zn-Ag Deposit in Fengning, Northern North China Craton: Constraints from Fluid Inclusions, H-O-S Isotopes and Fluorite Sr-Nd Isotopes. J. Earth Sci. 32 (1), 81–102. https://doi.org/10.1007/s12583-020-1393-8.

Yin, S., Ma, C.Q., Xu, J.N., 2017. Geochronology, geochemical and Sr–Nd–Hf-Pb isotopic compositions of the granitoids in the Yemaquan orefield, East Kunlun orogenic belt, northern Qinghai-Tibet Plateau: Implications for magmatic fractional crystallization and sub-solidus hydrothermal alteration. Lithos 294–295, 339–355. https://doi.org/10.1016/j.lithos.2017.10.012.

Yu, J.Z., Zheng, Y.Y., Xu, R.K., Hou, W.D., Cai, P.J., 2020. Zircon U-Pb chronology, geochemistry of Jiangjunmu ore-bearing pluton, Eastern part of East Kunlun and their geological significance. Earth Sci. 45 (4), 1151–1167 in Chinese with English abstract.

Yue, L., Jiao, Y.Q., Fayek, M., Wu, L.Q., Rong, H., 2021. Micromorphologies and sulfur isotopic compositions of pyrite in sandstone-hosted uranium deposits: A review and implications for ore genesis. Ore Geol. Rev. 139, 104512 https://doi.org/10.1016/j.oregeorev.2021.104512.

Zhai, D.G., Liu, J.J., Zhang, A.L., Sun, Y.Q., 2017. U-Pb, Re-Os, and 40Ar/39Ar Geochronology of Porphyry Sn ± Cu ± Mo and Polymetallic (Ag-Pb-Zn-Cu) Vein Mineralization at Bianjiadayuan, Inner Mongolia, Northeast China: Implications for Discrete Mineralization Events. Econ. Geol. 112 (8), 2041–2059. https://doi.org/10.5382/econgeo.2017.4540.

Zhai, D.G., Liu, J.J., Zhang, H.Y., Tombros, S., Zhang, A.L., 2018. A magmatic-hydrothermal origin for Ag-Pb-Zn vein formation at the Bianjiadayuan deposit, inner Mongolia, NE China: Evidences from fluid inclusion, stable (C-H-O) and noble gas isotope studies. Ore Geol. Rev. 101, 1–16. https://doi.org/10.1016/j.oregeorev.2018.07.005.

Zhai, D.G., Liu, J.J., Cook, N.J., Wang, X.L., Yang, Y.Q., Zhang, A.L., Jiao, Y.C., 2019. Mineralogical, textural, sulfur and lead isotope constraints on the origin of Ag-Pb-Zn mineralization at Bianjiadayuan, Inner Mongolia. NE China. Miner Deposita. 54 (1), 47–66. https://doi.org/10.1007/s00126-018-0804-6.

Zhai, D.G., Williams-Jones, A.E., Liu, J.J., Selby, D., Voudouris, P.C., Tombros, S., Li, K., Li, P.L., Sun, H.J., 2020. The Genesis of the Giant Shuangjianzishan Epithermal Ag-Pb-Zn Deposit, Inner Mongolia. Northeastern China. Econ Geol. 115 (1), 101–128. https://doi.org/10.5382/econgeo.4695.

Zhang, W.F., Deng, X., Peng, L.H., Zhang, Y., Xu, D.L., Liu, H., Jin, X.B., Sun, J., Lai, C., 2020. Rare earth elements and carbon-oxygen isotopes of calcite from the Tongjiachong Cu deposit, South China: Implications for fluid source and mineral precipitation. Ore Geol. Rev. 116, 103236 https://doi.org/10.1016/j.oregeorev.2019.103236.

Zhang, X.M., Zhao, X., Fu, L.B., Li, Y.J., Kamradt, A., Santosh, M., Xu, C.W., Huang, X.K., Borg, G., Wei, J.H., 2023. Crustal architecture and metallogeny associated with the Paleo-Tethys evolution in the Eastern Kunlun Orogenic Belt, Northern Tibetan Plateau. Geosci. Front. 101654 https://doi.org/10.1016/j.gsf.2023.101654.

Zhao, X., Fu, L.B., Wei, J.H., Bagas, L., Santosh, M., Liu, Y., Zhang, D.H., Zhou, H.Z., 2019. Late Permian back-arc extension of the eastern Paleo-Tethys Ocean: Evidence from the East Kunlun Orogen, Northern Tibetan Plateau. Lithos 340–341, 34–48. https://doi.org/10.1016/j.lithos.2019.05.006.

Zhao, X., Fu, L.B., Wei, J.H., Huizenga, J.M., Liu, Y., Chen, J.J., Wang, D.Z., 2021b. Generation and structural modification of the giant Kengdenongshe VMS-type Au-Ag-Pb-Zn polymetallic deposit in the East Kunlun Orogen, East Tethys: Constraints from geology, fluid inclusions, noble gas and stable isotopes. Ore Geol. Rev. 131, 104041 https://doi.org/10.1016/j.oregeorev.2021.104041.

Zhao, Y.H., Tian, H., Li, J., Chen, S.Y., Zhao, J.N., 2022. Constraints on the genesis of the Laochang Pb–Zn ore, Gejiu district, Yunnan: Evidence from sulfide trace element and isotope geochemistry. Ore Geol. Rev. 150, 105162 https://doi.org/10.1016/j.oregeorev.2022.105162.

Zhao, H.S., Wang, Q.F., Groves, D.I., Deng, J., 2021a. Progressive spatial and temporal evolution of tectonic triggers and metasomatized mantle lithosphere sources for orogenic gold mineralization in a Triassic convergent margin: Kunlun-Qinling Orogen, central China. GSA Bull. 133 (11–12), 2378–2392. https://doi.org/10.1130/B35754.1.

Zhong, S.H., Feng, C.Y., Seltmann, R., Li, D., 2017. Middle Devonian volcanic rocks in the Weibao Cu–Pb–Zn deposit, East Kunlun Mountains, NW China: Zircon chronology and tectonic implications. Ore Geol. Rev. 84, 309–327. https://doi.org/10.1016/j.oregeorev.2017.01.020.

Zhou, H.Z., Zhang, D.H., Wei, J.H., Wang, D.Z., Santosh, M., Shi, W.J., Chen, J.J., Zhao, X., 2020. Petrogenesis of Late Triassic mafic enclaves and host granodiorite in the Eastern Kunlun Orogenic Belt, China: Implications for the reworking of juvenile crust by delamination-induced asthenosphere upwelling. Gondwana Res. 84, 52–70. https://doi.org/10.1016/j.gr.2020.02.012.

Zhu, D.P., Li, H., Tamehe, L.S., Jiang, W.C., Wang, C., Wu, K.Y., 2022. Two-stage Cu Pb Zn mineralization of the Baoshan deposit in southern Hunan, South China: Constraints from zircon and pyrite geochronology and geochemistry. J. Geochem. Explor. 241, 107070 https://doi.org/10.1016/j.gexplo.2022.107070.

Zong, K.Q., Klemd, R., Yuan, Y., He, Z.Y., Guo, J.L., Shi, X.L., Liu, Y.S., Hu, Z.C., Zhang, Z.M., 2017. The assembly of Rodinia: The correlation of early Neoproterozoic (ca. 900 Ma) high-grade metamorphism and continental arc formation in the southern Beishan Orogen, southern Central Asian Orogenic Belt (CAOB). Precambr. Res. 290, 32–48. https://doi.org/10.1016/j.precamres.2016.12.010.